

1 **The Sediment Budget Estimator (SBE): a process-model for the stochastic estimation**  
2 **of fluxes and budgets of sediment through submarine channel systems.**

3

4 Eggenhuisen, J.T.<sup>1\*</sup>, Tilston, M.C.<sup>2</sup>, Stevenson, C.J.<sup>3</sup>, Hubbard, S.M.<sup>2</sup>, Cartigny, M.J.B.<sup>4</sup>, Heijnen, M.S.<sup>5</sup>,  
5 de Leeuw, J.<sup>1</sup>, Pohl, F.<sup>6</sup>, and Spychala, Y.T.<sup>7</sup>

6

7 \*corresponding author: [j.t.eggenhuisen@uu.nl](mailto:j.t.eggenhuisen@uu.nl)

8 <sup>1</sup>Faculty of Geosciences, Utrecht University, the Netherlands.

9 <sup>2</sup>Department of Geoscience, University of Calgary, Canada.

10 <sup>3</sup>School of Environmental Sciences, University of Liverpool, United Kingdom.

11 <sup>4</sup>Departments of Earth Science and Geography, Durham University, United Kingdom.

12 <sup>5</sup>Ocean and Earth Science, University of Southampton, United Kingdom.

13 <sup>6</sup>School of Biological and Marine Sciences, University of Plymouth, United Kingdom.

14 <sup>7</sup>Institute of Geology, Leibniz University Hannover, Germany.

15

16 This is a preprint submitted to EarthArXiv. The manuscript has been revised following a first round of  
17 peer-review performed for the *Journal of Sedimentary Research*, where it has been re-submitted. As  
18 this manuscript still has to undergo further peer-review, subsequent versions may have different  
19 content. If accepted, the final version of this manuscript will be available via the 'Peer-reviewed  
20 Publication DOI' link on the right hand side of this webpage. Please feel free to contact the  
21 corresponding author directly regarding this manuscript.

22

## ABSTRACT

23  
24 Turbidity currents transport vast amounts of sediment through submarine channels onto deep-  
25 marine basin floor fans. There is a lack of quantitative tools for the reconstruction of the sediment  
26 budget of these systems. The aim of this paper is to construct a simple and user-friendly model that  
27 can estimate turbidity-current structure and sediment budget based on observable submarine  
28 channel dimensions and general characteristics of the system of interest. The requirements for the  
29 model were defined in the spirit of the source-to-sink perspective of sediment volume modeling: a  
30 simple, quantitative model that reflects natural variability and can be applied to ancient systems with  
31 sparse data-availability. The model uses the input conditions to parameterize analytical formulations  
32 for the velocity and concentration profiles of turbidity currents. Channel cross-section and temporal  
33 punctuation of turbidity-current activity in the channel are used to estimate sediment flux and  
34 sediment budget. The inherent uncertainties of geological sediment budget estimations motivate a  
35 stochastic approach, which results in histograms of sediment budget estimations, rather than  
36 discrete values. The model is validated against small-scale experimental turbidity currents and the  
37 1929 Grand Banks turbidity current. The model performs within acceptable margins of error for  
38 sediment flux predictions at these smallest and largest scales of turbidity currents possible on Earth.  
39 Finally, the model is applied to reconstruct the sediment budget related to Cretaceous slope-channel  
40 deposits (Tres Pasos Formation, Chile). The results give insight into the likely highly stratified  
41 concentration profile and the flow velocity of the Cretaceous turbidity currents that formed the  
42 deposits. They also yield estimates of the typical volume of sediment transported through the  
43 channels while they were active. These volumes are demonstrated to vary greatly depending on the  
44 geologic interpretation of the relation between observable deposit geometries and the dimensions  
45 of the flows that formed them. Finally, the shape of the probability density functions of predicted  
46 sediment budgets is shown to depend on the geological (un)certainty ranges. Correct geological  
47 interpretations of deep marine deposits are therefore indispensable for quantifications of sediment  
48 budgets in deep marine systems.

49

## INTRODUCTION

50 The rationale in studies about turbidity currents and their deposits often refers to submarine fans  
51 being the most voluminous sedimentary bodies on Earth (Middleton, 1993) and turbidity currents  
52 the most prolific transport agents on the planet (Talling *et al.*, 2012), yet no study has succeeded in  
53 presenting a process model that can be used to relate the turbidity currents responsible for the flux  
54 of sediment to the volumes of submarine fan deposits (Jobe *et al.*, 2018). The budget of sediment  
55 transported onto submarine fans is governed by geological mechanisms that operate on thousands  
56 to millions of years involving climate, tectonics, and sea level variations, and it is measured in cubic  
57 kilometers [km<sup>3</sup>]. The flux of sediment in turbidity currents is governed by complex particle-fluid  
58 dynamics operating on milliseconds to hours, and it is measured in cubic meters per second [m<sup>3</sup>/s].  
59 This disparate spread in scales and types of controls makes calculation of geological sediment  
60 budgets from flow processes one of the big challenges in marine geosciences.

61 The source-to-sink approach to studying the entire geological chain of sediment production and  
62 transport has gained prominence in the past decade. It holistically tracks the budget of sediment  
63 from weathering of bedrock in mountainous or hilly catchment areas (the source), through the  
64 various depositional environments along the transport path, all the way to the terminal depositional  
65 sink in the deep oceans (Sømme *et al.*, 2009a; Walsh *et al.*, 2016). A strength of the source-to-sink  
66 approach has been that it made the ultimate simplification of the process of sediment transport,  
67 while still yielding robust and informative answers to geological problems. Sediment is simply  
68 distributed from the source to the sink, and the various depositional sub-systems that are passed  
69 along the pathway (rivers, deltas, the continental shelf) act to extract a certain fraction of the  
70 available sediment budget (Paola & Martin, 2012). This success may be counterintuitive when  
71 observed parallel to the development of process-based modelling efforts that seek increasingly more  
72 detailed and complex treatments of the dynamics of sediment transport (Cantero *et al.*, 2011; Abd El-  
73 Gawad *et al.*, 2012; Basani *et al.*, 2014; Kneller *et al.*, 2016). Herein we explore how turbidity-current  
74 processes can be incorporated in a source-to-sink approach without decreasing its robustness and

75 viability. Such incorporation of process-modelling into source-to-sink studies is one of the key areas  
76 for future advances suggested by Walsh et al. (2016) and Romans et al. (2016) in their reviews of the  
77 past, present, and future of the source-to-sink perspective. Geological uncertainties in source-to-sink  
78 analyses are commonly large (Sømme *et al.*, 2009a), which means that boundary conditions for  
79 model simulations are defined as probable ranges, rather than specific values. We argue that this  
80 requires using stochastic process-modelling approaches to predictions of fluxes of sediment into  
81 deep water.

82 The objective of this study is to construct a simple and user-friendly model that can estimate  
83 turbidity current parameters and sediment budgets based on observable submarine channel  
84 parameters. This geological tool should account for natural variability and be applicable to ancient  
85 systems (Sømme and Martinsen, 2017). The result is the Sediment Budget Estimator (SBE), a process-  
86 based turbidity-current model that predicts sediment budget transferred through submarine  
87 channels from the continental slope to submarine fans over geological timescales. The essence of the  
88 SBE approach is similar to the paleohydrologic “fulcrum approach” to fluvial sediment-budget  
89 estimation as proposed by (Holbrook & Wanas, 2014) and applied by (Lin & Bhattacharya, 2017;  
90 Sharma *et al.*, 2017). The fulcrum method perceives a fluvial channel cross section as the pivot  
91 between the sediment load received from the up-stream domain and transmitted to a downstream  
92 domain. It analyzes the relation between local channel-fill deposit architecture and the expected  
93 sediment throughput. In this paper we will describe this model-approach with special emphasis on  
94 the connection between flow structures of turbidity currents, their specific geological basin setting,  
95 and the geometry of submarine channels. Consideration will be given to deep-marine concepts that  
96 can be used to constrain simulations. The model is then validated against the smallest and largest  
97 scales of sediment delivery into deep basins for which accurate dynamic data are available:  
98 laboratory scale turbidity currents (de Leeuw *et al.*, 2016, 2018b) and the 1929 Grand Banks turbidity  
99 current (Heezen & Ewing, 1952; Kuenen, 1952; Stevenson *et al.*, 2018). Finally, the model is applied  
100 to estimate the sediment budget associated with Cretaceous submarine channel deposits exposed in

101 the Tres Pasos Formation in Southern Chile (Hubbard *et al.*, 2010, 2014; Macauley & Hubbard, 2013;  
102 Hubbard *et al.*, 2020). This application demonstrates the importance of geological models derived  
103 from stratigraphic observations for sediment budget estimations. The statistical uncertainties in  
104 sediment budget estimates on geologic time-scales can be decreased by narrowing the confidence  
105 bounds through scrutiny of the geologic record. Hence, the predictability of source-to-sink transfer of  
106 sediment to the terminal depositional sink in the deep oceans depends on the strength and  
107 confidence of geological models.

108

#### 109 **METHODOLOGY: FORMULATION OF THE TURBIDITY CURRENT FLOW-STRUCTURE MODEL**

110 The backbone of the SBE is formed by analytical formulations for vertical profiles of velocity,  $u(z)$ , and  
111 concentration,  $c(z)$ , in turbidity currents (Fig. 1a). These are coupled by two closure equations that  
112 relate the velocity and concentration in the flow: 1) a sediment bypass condition that relates the  
113 shear velocity to the basal sediment concentration (Eggenhuisen *et al.*, 2017); and 2) a conventional  
114 formulation that relates the average sediment concentration to the shear velocity (e.g. Kneller, 2003;  
115 García, 2008).

116

#### 117 *Velocity Profile*

118 The velocity profile of turbidity currents has been recognized to display robust, recurring patterns  
119 (Plapp & Mitchell, 1960; Stacey & Bowen, 1988; Garcia & Parker, 1993; Altinakar *et al.*, 1996; Kneller  
120 *et al.*, 1999; Kneller & Buckee, 2000; Best *et al.*, 2001; Xu *et al.*, 2002; Gray *et al.*, 2005; Straub *et al.*,  
121 2008; Islam & Imran, 2010; Sequeiros *et al.*, 2010; Xu, 2011; Eggenhuisen & McCaffrey, 2012;  
122 Sequeiros, 2012; Cartigny *et al.*, 2013; Cooper, 2013; Pittaluga & Imran, 2014; Azpiroz-Zabala *et al.*,  
123 2017; Sequeiros *et al.*, 2018). This robustness of the shape of the velocity profile results from the  
124 simple essential structure of turbidity currents: the bottom boundary is assumed to be a turbulent,  
125 wall-bound, shear layer; and the upper boundary is a turbulent mixing layer between the turbidity  
126 current and the ambient fluid. The velocity model developed here is therefore formed by the

127 addition of two velocity functions: the logarithmic law of the wall, and a plane-mixing-layer velocity  
 128 function. Different approaches have been proposed for the effective superposition of these functions  
 129 (Altinakar *et al.*, 1996; Kneller *et al.*, 1999).

130 We follow the approach of Kneller *et al.* (1999) by assuming a logarithmic velocity profile from the  
 131 bed to the flow depth, and applying a mixing layer structure throughout the water column (Fig. 2).

132 We deviate slightly from Kneller *et al.* (1999) who use the “interface” between sediment laden and  
 133 clear water as the flow depth. This interface can be qualitatively observed instantaneously in  
 134 turbidity currents, e.g. in pictures of experiments, but due to the multitude of turbulent mixing  
 135 structures passing any one location over time it cannot be quantitatively defined in a time-averaged  
 136 structure of a turbidity current, where the velocity and concentration asymptotically approach 0 with  
 137 height (Garcia & Parker, 1989; Islam & Imran, 2010; Sequeiros *et al.*, 2010; de Leeuw *et al.*, 2018a).  
 138 Instead, we follow Hermidas *et al.* (2018) by defining the elevation  $z=H$  as the center of mixing layer  
 139 and top of the logarithmic profile (Fig. 2), where  $z$  is the bed perpendicular coordinate. This measure  
 140 of flow depth ( $H$ ) is equated to levee height ( $D$ ) in our approach (Fig. 1B). This definition is a key  
 141 aspect of the modelling strategy, and will be further justified below.

142 The velocity  $u$  [m/s] as a function of elevation above the bed  $z$  [m] is then:

$$143 \quad u(z) = u_{\log}(z) - u_{PML}(z) \quad (1)$$

144 The logarithmic velocity function is:

$$145 \quad u_{\log}(z) = \frac{u^*}{\kappa} \ln \left( \frac{z}{z_0} \right) \Big|_{z_0 \leq z \leq H} \quad (2)$$

$$u_{\log}(z) = \frac{u^*}{\kappa} \ln \left( \frac{H}{z_0} \right) \Big|_{z \geq H}$$

146 Where  $u^*$  is the shear velocity [m/s],  $\kappa$  is von Karman’s constant [0.4],  $z$  is the bed-perpendicular  
 147 coordinate, and  $z_0$  is the elevation at which the turbulent velocity profile intersects 0 m/s (Van Rijn,  
 148 2011).

149 The non-dimensional velocity distributions of plane mixing layers collapse into a universal function  
150 with the form (Champagne *et al.*, 1976; Pope, 2000):

$$151 \quad f(\xi) = 1/2 \operatorname{erf}\left(\frac{\xi}{\sigma\sqrt{2}}\right) \quad (3)$$

152 Where  $\sigma$  has been analytically determined to be  $\sim 0.39$  (Pope, 2000), and  $\xi$  is a non-dimensional  
153 coordinate perpendicular to the bed:

$$154 \quad \xi = (z - z_{50}) / (z_{10} - z_{90}) \quad (4)$$

155 The subscripts denote the elevations of the velocity percentiles, e.g.  $z_{50}$  is the z-coordinate where the  
156 velocity is equal to 50% of the maximum velocity ( $u_{log}(H)$ ). The range between  $z_{10}$  and  $z_{90}$  is  
157 approximated closely by  $H$  (Pope, 2000).

158 The scaled velocity function  $f(\xi)$  relates to the dimensional plane-mixing-layer velocity function as:

$$159 \quad u_{PML}(\xi) = u_{log}(H) [f(\xi) + 1/2] \quad (5)$$

160 Note that the plane mixing layer is scaled with the logarithmic velocity, not with the velocity  
161 maximum of the turbidity current (Kneller *et al.*, 1999). The maximum velocity, as well as the  
162 elevation of the maximum velocity of the turbidity current thus arise from the modelling, and are not  
163 constrained *a priori*. Equation 5 mathematically extends below the bed where it asymptotically  
164 approaches 0. The residual velocity of Eq. 5 at  $z=0$  is 0.1% of  $u_{log}(H)$ , which is deemed insignificant for  
165 the purpose of modelling the sediment budget of submarine channel systems.

166

### 167 *Concentration Profile*

168 The shape of the concentration profile of many experiments is a rather similar, slightly concave  
169 exponential function (Garcia, 1994; Choux *et al.*, 2005; Islam & Imran, 2010; Sequeiros *et al.*, 2010;  
170 Tilston *et al.*, 2015; de Leeuw *et al.*, 2018a). The concentration function is here expressed in the  
171 simplest form of an exponential decay function:

$$172 \quad c(z) = C_b e^{-kz} \quad (6)$$

173 Where  $c(z)$  is the sediment concentration at elevation  $z$  [m],  $C_b$  is the sediment concentration at the  
174 base of the flow [-], and  $k$  is a decay constant [1/m].

175

### 176 *Closure Relations Between Variables*

177 **Sediment Bypass Closure** --- Submarine channels are effective bypass conduits for sediment  
178 into deep basins (Stevenson *et al.*, 2015; Kneller *et al.*, 2016) that remain open conduits for most of  
179 their lifespan (Hubbard *et al.*, 2014), such that the sediment mass eventually deposited in the  
180 channel-fill deposits at a given cross section represents only a minute portion of the sediment mass  
181 transported through that cross section (Paola & Martin, 2012; Stevenson *et al.*, 2015; de Leeuw *et al.*,  
182 2018b). A bypass condition is therefore used here to reconstruct the characteristic sediment flux  
183 going through a channel. The bypass condition is here based on the suspension capacity parameter  $\Gamma$   
184 of Eggenhuisen *et al.* (2017), which balances the gravitational, buoyancy and turbulent forces acting  
185 on the suspended load. It includes universal turbulent flow scales and material properties of the  
186 fluid and particles only. The condition  $\Gamma < 1$  coincides with the complete consumption of bed-  
187 generated turbulence by sediment suspension, as observed in direct numerical simulations (Cantero  
188 *et al.*, 2009, 2011, 2012). This over-saturated sediment condition is thought to lead to rapid  
189 deposition. The condition  $\Gamma = 1$  can be used to relate the sediment concentration at the base of a  
190 bypassing turbidity current  $C_b$  to flow conditions and material properties of water and sediment  
191 (Eggenhuisen *et al.*, 2017):

$$192 \quad C_b = \frac{u_*^3}{140\nu g R} \quad (7)$$

193 Where  $\nu$  [m<sup>2</sup>/s] is the kinematic viscosity of water,  $g$  [m/s<sup>2</sup>] is the acceleration by gravity, and  $R$  [-] is  
194 the submerged relative density of quartz in water (1.65).

195 **Parameterization of the Logarithmic Velocity Profile** --- Shear velocity and  $z_0$  are the two  
196 parameters that are needed to resolve the logarithmic velocity function (Eq. 2).



197 The shear velocity is estimated from the shear stress at the base of the flow due the excess weight of  
 198 suspended sediment:

$$199 \quad u^* = \sqrt{H_r \bar{C} g R S} \quad (8)$$

200 Where  $H_r$  is the hydraulic radius [m], which is calculated as the cross-sectional area divided by the  
 201 frictional perimeter. The interface with the ambient fluid is included into the frictional perimeter  
 202 here.  $\bar{C}$  is the input depth-averaged sediment concentration [-], which is evaluated between the bed  
 203 and  $z=H$  (see Boundary Conditions, below).  $S$  is the tangent of the slope [-].

204 Different empiric relations have been suggested for  $z_0$  (Garcia, 2008; van Rijn, 2011). In the version  
 205 used here, a distinction is made between mobile and non-mobile beds, based on the ratio between  
 206 the bed shear stress ( $\tau_b$ ) and the critical bed shear stress ( $\tau_c$ ) for initiation of transport of the bed  
 207 material (“transport stage” *sensu* van Rijn, 2011):

$$208 \quad z_0 = \frac{k_s}{30} + \frac{\nu}{9u^*} \Big|_{\tau_b < \tau_c} \quad (9)$$

$$z_0 = \frac{k_s}{30} + \delta_b \Big|_{\tau_b \geq \tau_c}$$

209 Where  $k_s$  is the Nikuradse equivalent sand roughness [m], and  $\delta_b$  is the thickness of the bedload  
 210 layer [m]. The Nikuradse equivalent sand roughness can be estimated from the grainsize of the  
 211 coarsest sediment particles on the bed ( $d_{90}$ ; 90<sup>th</sup> percentile of the grainsize distribution; van Rijn,  
 212 2011):

$$213 \quad k_s \approx 3d_{90} (\textit{sand}) \quad (10)$$

$$k_s \approx d_{90} (\textit{gravel})$$

214 The thickness of the bedload layer is estimated as (Garcia, 2008):

$$215 \quad \delta_b = \frac{0.015d_{50}[\tau_b/\tau_c]}{1 + 0.2[\tau_b/\tau_c]}$$

216 Where  $d_{50}$  is the median grainsize of the bed material [m]. Form roughness effects related to  
 217 irregular shapes of the bed (e.g. bedforms) are not incorporated in Eq. 9.

218

219

### *Boundary Conditions*

220 The structure of equations 1-10 has been chosen such that they can now be solved when boundary  
221 condition values are set for flow thickness  $H$ , depth averaged sediment concentration  $\bar{C}$ , slope  $S$ ,  
222 and characteristic bed-grainsize, which are all variables that deep marine geologists can estimate and  
223 debate. The probabilistic nature of the SBE will allow the users to rapidly test their ideas on the  
224 confidence bounds of these parameters. It is thus not necessary to know exactly how thick  
225 characteristic turbidity currents in a system of interest are, nor what their average concentration  
226 was. Rather, the model can be used to test how these parameters affect predictions of sediment  
227 fluxes and budgets. This probabilistic functionality requires the user to define a range between likely  
228 minimum and maximum values for each of the boundary conditions. These ranges are uniformly  
229 sampled by the SBE with a user-defined number of steps in between the minimum and maximum  
230 values. Equations 1-10 are solved for all combinations of each of the boundary condition values. This  
231 can lead tens of thousands turbidity currents being simulated at a given cross-section.

232

233 **Flow Thickness Correlates to Channel Depth** --- Turbidity current thickness is often assumed  
234 to be closely related to the depth of the channel in modelling approaches (Salles *et al.*, 2009; Abd El-  
235 Gawad *et al.*, 2012; Arfaie *et al.*, 2014; Basani *et al.*, 2014; Hamilton *et al.*, 2017; Jobe *et al.*, 2017;  
236 Kane *et al.*, 2017). Such bank-full discharge assumptions are common in fluvial paleohydrology, but  
237 much less straightforward in channelized turbidity currents, which may extend above the levee crest  
238 while most of the sandy sediment is bypassed in proximity to the channel floor (Hiscott *et al.*, 1997).  
239 This key assumption will therefore be addressed in depth.

240 Firstly, the simple argument of scale is supported by the validity of laboratory modelling of  
241 channelized turbidity current morphodynamics (de Leeuw *et al.*, 2016), which demonstrates that  
242 laboratory-sized flows that are orders of magnitude smaller than real world flows self-generate  
243 channels at similar dimensions to the flows: small turbidity currents build small channels and large  
244 turbidity currents build large channels.

245 Furthermore, our morphodynamic understanding of levee-building includes a self-regulatory  
246 mechanism, whereby the levees aggrade by deposition from the dilute top of the flow, causing the  
247 levee-building to halt when the channel relief reaches a similar scale as the flow thickness (Straub &  
248 Mohrig, 2008; Shumaker et al., 2018)). Indeed, the variability of flow thickness with respect to  
249 channel dimensions has been argued to be small by Straub et al. (2008) who suggest that the channel  
250 form and flow scale are tuned to each other. The robustness of this self-regulatory mechanism is  
251 reflected in the successful application of the geomorphological concept of hydraulic geometry  
252 (Leopold & Maddock, 1953) to submarine channels by Konsoer et al. (2013), who established that a  
253 correlative power-law relation between turbidity current discharge and submarine channel  
254 dimensions does exist.

255 Investigating the process of channelized flow in more detail, Mohrig and Buttles (2007) established  
256 experimentally that channels serve as effective conduits for turbidity currents that are 1.3 times  
257 thicker than the channel-form is deep. The along-axis flow velocities are an order of magnitude  
258 higher than the cross-channel overspill velocity in such confined flows. The ratio of along-axis to  
259 cross-channel velocity rapidly decreases for partially confined flows that are thicker than 1.3 times  
260 the channel depth (Mohrig & Buttles, 2007), indicating that those flows are poorly confined by the  
261 channel and rapidly spread out over the overbank area. Mohrig and Buttles (2007) use a  
262 conventional definition of flow thickness as the distance between the bed and an interface between  
263 ambient fluid and the turbidity current ( $H_{MB}$ ). This interface is not defined in a time-averaged velocity  
264 profile, and falls somewhere in the top half of the mixing layer. The proposal of Hermidas et al.  
265 (2018) to define the center of the mixing layer as the flow depth (Fig. 2) is less ambiguous and more  
266 straightforward: the simple condition of  $H=D$  (Fig. 1a&b) is roughly equal to the regime-boundary for  
267 fully channelized flows as defined by Mohrig and Buttles (2007), because  $H_{MB}=1.3*D$ , and  $H=D$  here.  
268 Finally, the bypass condition based on the suspension capacity parameter of Eggenhuisen et al.  
269 (2017) also contains a mechanism that causes channel dimensions to be attracted to a bypass state  
270 for the characteristic turbidity currents in the system. If the concentration at the base of the flow

271 exceeds the saturation concentration, this will lead to the immediate deposition of excess sediment  
272 on the bed, until  $\Gamma = 1$ . This will partially fill the channel form, decreasing levee height to re-  
273 equilibrate channel dimensions with smaller characteristic turbidity currents (Shumaker *et al.*, 2018).  
274 If the concentration falls below the saturation concentration, there is excess suspension capacity that  
275 will lead to entrainment of sediment from the channel floor. This will increase the depth and cross-  
276 sectional area of the channel to re-equilibrate with the size of larger characteristic turbidity currents.  
277 In conclusion, a diverse suite of concepts suggests that channel size and thickness of characteristic  
278 turbidity currents are related to each other, and this justifies the equation of channel depth and flow  
279 thickness ( $H=D$ ) in the first order prediction of flow structures from channel dimensions.

280

281 **Concentration: the Density of the Turbidity Current** --- Robust first order predictability of  
282 concentration magnitude through wholly process-based equations in this simplified model  
283 framework is not yet feasible. The choice is therefore made here to make the average concentration  
284 a user-defined boundary condition, rather than set it through some empiric parameters behind the  
285 scenes of the SBE. This approach at least makes the concentration uncertainty clearly defined by the  
286 user at the front end of the model. The question now arises what typical concentrations are of  
287 turbidity currents.

288 Measurements of concentration profiles of real-world turbidity currents were published by Azpiroz-  
289 Zabala *et al.* (2017) and Simmons *et al.* (2020). They recorded very low depth-averaged  
290 concentrations of 0.017-0.023 % in 48-77m thick turbidity currents travelling down the Congo  
291 Canyon with a velocity of under 1 m/s. These conditions are likely to represent the slower end of the  
292 spectrum of turbidity currents in the Congo Canyon, though other measurement attempts of faster  
293 events have so far resulted in equipment failures (Khripounoff *et al.*, 2003). Reliable average  
294 concentration measurements are not available for such faster natural turbidity currents in other  
295 systems either. Due to the near-complete lack of accurate concentration profile measurements in  
296 natural flows (Wang *et al.*, 2020), various authors have tried to estimate average concentrations by

297 combining other variables with equations. Konsoer et al. (2013) combine friction factor estimates  
298 with estimations of bank full conditions that are much like the perspective set out in the previous  
299 section. This leads them to estimate a sediment concentration range of 0.2-0.6% for a selection of  
300 channels exposed on the modern sea floor. Zeng et al. (1991) also applied friction factors to estimate  
301 sediment concentration during a turbidity current that occurred in May 1986 in the submarine  
302 channel in Bute Inlet (Canada). This turbidity current travelled at 3.6 m/s, resulting in a sediment  
303 concentration estimate of 0.5-0.7% (Zeng et al., 1991). These depth-averaged concentration values  
304 seem to be more representative for a broader range of active and ancient turbidity current systems  
305 than the very dilute concentrations reported by Azpiroz-Zabala et al. (2017) for the Congo Canyon.  
306 Indeed, a compilation by Sequeiros (2012) of concentration estimations from literature leads the  
307 author to suggest that 0.45% is a typical average concentration at field scale, consistent with both  
308 the range suggested by Konsoer et al. (2013), and the estimate of Zeng et al. (1991). Finally, the  
309 Grand Banks 1929 turbidity current was the single largest turbidity current event known to have  
310 occurred in modern times, and its size, velocity, and sediment concentration have historically been  
311 thought of as the upper limits of what is possible in oceans on Earth (Kuenen, 1952). The sediment  
312 concentration was estimated to be 1.1-2.9% (Plapp and Mitchell, 1966), an estimate that has recently  
313 been adjusted to 2.7-5.4% (Stevenson et al., 2018; see below). This upper concentration limit is  
314 consistent with the review by Sequeiros (2012), who suggests that the average sediment  
315 concentration of a turbidity current rarely exceeds 5%.

316 Based on these sources, we suggest the following broad subdivisions for the average input  
317 concentration in SBE simulations (Table 1): very dilute [0.05-0.2%]; dilute [0.2-0.6%]; intermediate  
318 [0.6-2%]; high [2-5%], with the dilute range advisable as a default. Interestingly, Reginald Daly arrived  
319 at likely sediment concentrations of 0.3-0.6% in his rather brilliant 1936 paper, solely by applying  
320 deductive and partially intuitive reasoning (Daly, 1936). The “high” concentration class suggested  
321 here is considerably lower than the >10-15% concentration suggested for “high-density turbidity  
322 currents” by Lowe (1982). The apparent discrepancy likely arises because Lowe considered processes

323 occurring at the base of turbidity currents, where sediment concentrations can be much higher than  
324 the depth averaged concentration. Indeed, observations in Monterey Canyon (Paull *et al.*, 2018)  
325 support a model for high-density turbidity currents where a dense basal layer of up to a few meters  
326 thick, with sediment concentrations far exceeding 10%, is overlain by a thicker, dilute cloud.  
327 The user defined depth-averaged concentration allows evaluation of the following integral in the  
328 model workflow:

$$329 \quad \overline{CH} = \int_0^{\infty} C_b e^{-kz} dz \quad (11)$$

330 Evaluation of the integral results in an expression of the decay constant  $k$ :

$$331 \quad k = \frac{C_b}{\overline{C}} \frac{1}{H} \quad (12)$$

332 The decay constant thus depends on flow thickness, and the ratio of near-bed concentration to  
333 average concentration. This ratio often appears in modelling studies of turbidity currents (Parker *et al.*  
334 *et al.*, 1986; Halsey *et al.*, 2017). It is the simplest measure for the degree of density stratification in the  
335 turbidity current. It approaches 2 in many experiments (Parker *et al.*, 1987), while higher numbers  
336 have been proposed, and recently confirmed, for natural scale flows (Azpriez-Zabala *et al.*, 2017;  
337 Simmons *et al.*, 2020). Note that the concentration profile as described by Eq. 6 asymptotically  
338 approaches 0 at an indefinite elevation above the channel floor; some of the sediment declared in  
339 the two boundary conditions  $\overline{CH}$  is thus actually suspended above the bank-full elevation in the  
340 exponential concentration profile. The chosen structure of Eq. 11 therefore creates a discrepancy  
341 between the average concentration between the channel floor and the bank full depth, and the  
342 average of Eq. 6 between these two levels. A similar effect occurs in the more common integral  
343 approach of Ellison and Turner (1959). The magnitude of this error depends on the vertical gradient  
344 of sediment concentration near the top of the flow, and is negligible in natural currents that have low  
345 concentrations with almost no gradient at elevation  $H$  (see for example Fig. 3b).

346

347 **Slope of the System** --- The slope of a channel is well defined in medium-low resolution  
348 oceanographic datasets. In subsurface systems, the slope can be estimated from seismic datasets  
349 (Shumaker *et al.*, 2017; Beelen *et al.*, 2019). If data does not allow the slope to be measured directly  
350 for a system, slope estimates can also be based on analogues from modern oceanography (Covault *et*  
351 *al.*, 2011; Prather *et al.*, 2016) or stratigraphic panels of outcrop systems (Johannessen & Steel, 2005;  
352 Hubbard *et al.*, 2010; Daniels *et al.*, 2018). Compaction of clinoforms adds an extra source of  
353 uncertainty (Beelen *et al.*, 2019) that can be taken into account when setting the confidence bounds  
354 of the slope values. Helland-Hansen *et al.* (2016) qualitatively grouped system styles with different  
355 steepness (Helland-Hansen *et al.*, 2016), and quantifications of the slope steepness have also  
356 recently been reviewed (Patruno *et al.*, 2015; Patruno & Helland-Hansen, 2018). Based on these  
357 sources, users of the SBE could use the following classes if no slope data is available for their system  
358 of interest (Table 1): Gentle: 0.5-1°; Intermediate: 1-2.5°; Steep: 2.5-6°; Very Steep 6-12°. The very-  
359 steep class appears to be relevant only for steep submarine canyon systems, such as the Var Canyon  
360 (Mulder *et al.*, 1998), the canyons in the Ebro and North Catalan margins (Amblas *et al.*, 2006; Lastras  
361 *et al.*, 2011), or some canyons on the North American Pacific Margin (Lee *et al.*, 2002).

362

363 **Bed Roughness** --- The size of the coarsest sediment particles making up the bed determines  
364 the bed roughness, which provides a boundary condition needed to solve Eqs. 10, 9, and 2. The user  
365 is therefore required to supply an estimation of the coarse fraction of the sediment particles present  
366 on the channel thalweg. This data can be obtained from grain-size analysis of core-samples obtained  
367 from the channel under investigation. It can also be taken from samples within other parts of the  
368 system when the channel body itself has not been cored, though this approach could lead to under-  
369 estimation of the grain size in the channel thalweg. No grain-size samples may be available in  
370 exploration settings. Geologists will then generally be able to set likely values (e.g. Table 1) based on  
371 their understanding of the basin setting and the source area of the sediment (Reading & Richards,  
372 1994; Richards *et al.*, 1998).

373

374

## METHODOLOGY: THE SEDIMENT FLUX [M<sup>3</sup>/S] AND BUDGET [KM<sup>3</sup>] MODULES

375

376

### *From Flow Structure to Sediment Flux*

377

The sediment flux per unit width by the characteristic turbidity current can be determined by

378

multiplying the concentration at each elevation with the corresponding velocity and integrating from

379

the bed to an elevation some distance above the channel (Plapp & Mitchell, 1960):

380

$$Flux_{1D} = \int_0^{\infty} c(z)u(z)dz \quad (12)$$

381

The vertical coordinate is discretized in the SBE with steps of size  $\Delta z$ , such that this expression can be

382

evaluated as the dot product of the concentration and velocity profiles multiplied by the vertical step

383

size:

384

$$Flux_{1D} = c(z) \bullet u(z) \Delta z \quad (13)$$

385

The units of this sediment flux per unit width are m<sup>2</sup>/s. The channel cross-section is here simplified to

386

a trapezoidal shape, consisting of a flat channel-thalweg section in the middle, and two channel

387

margins on either side (Fig. 1c). The lateral channel-bank angle is user defined, but will be set to 10

388

degrees throughout this paper for simplicity. The estimation of the total sediment flux through the

389

channel cross section follows a procedure established in fluvial processes and engineering (Chang,

390

1988): For each section in the trapezoidal cross section, we calculate a hydraulic radius, shear

391

velocity, and velocity and concentration profiles. The resulting flux of Eq. 13 is multiplied by the

392

section-width, and the section-fluxes are added to obtain the total sediment flux through the channel

393

cross-section [m<sup>3</sup>/s]. The section-method can be used to calculate fluxes through more sophisticated

394

cross-sectional channel shapes, for instance by calculating turbidity current structures that represent

395

more (e.g. 10) lateral channel sections within a single channel cross section. This is not pursued here,

396

because this is deemed to only give second order improvements in predicting the sediment flux at

397

the cost of an order of magnitude increase in amount of turbidity current structures that need to be



398 calculated. The added demand on the specificity of boundary condition constraints, in this case the  
399 channel cross-sectional shape, is also contrary to the philosophy of the SBE.

400

#### 401 *From Sediment Flux to Sediment Budget*

402 The sediment supply to deep-water sedimentary systems is punctuated on the time scales of events  
403 and geological cycles (Romans *et al.*, 2016). The geological sediment budget needs to be calculated  
404 by multiplying sediment flux of the characteristic turbidity currents with the typical duration of a  
405 typical flow event, its frequency, and the (geologic) time-scale of the system's activity. The sediment  
406 budget is reported by the SBE, and throughout this paper, as the volume of sediment only, *excluding*  
407 porosity of related deposits.

408

409 **Turbidity Current Duration** --- Turbidity currents have been estimated from turbidite  
410 deposits to last minutes to hours in various ways (Piper *et al.*, 1988, [minimum 2 hours]; Allen, 1991,  
411 [20-52 minutes]; Baas *et al.*, 2000, [16-19 minutes]; Jobe *et al.*, 2012, [3-176 minutes]; Jobe *et al.*,  
412 2017, [minimum 6-12 minutes]; Stevenson *et al.*, 2018, [4-8 hours]). Measurements of turbidity  
413 currents indicate that flows last minutes on proximal delta slopes (Hughes Clark, 2016). The majority  
414 of monitored flows in upper canyons, however, last between 1-10 hours (see Talling *et al.*, 2013 for a  
415 review). Measurements in the Congo Canyon, which is the only of the major passive-margin deep  
416 water systems that is presently active, show that flows last up to 10 days 170 km away from the  
417 canyon head at water depths of 2000 m (Cooper, 2013; Azpiroz-Zabala *et al.*, 2017). This longer flow  
418 duration in a major canyon system is consistent with the estimation for the Pleistocene Amazon  
419 flows by Pirmez and Imran (2003). They estimated that flows lasted several days in the Pleistocene  
420 phase of activity of the Amazon fan. These measurements and estimations are in line with the  
421 suggestion by Azpiroz-Zabala *et al.* (2017) that turbidity current duration is a function of distance  
422 from the source area of the flows and the stretching of flows as they transit down the system. The  
423 transit time of a flow towards a location in the basin allows the flow to stretch due to different

424 velocities in different parts of the flow. Flows therefore last longer further away from the source, and  
425 similarly they last longer in the distal sections of larger systems. Even the very long turbidity currents  
426 measured in the Congo Canyon can be explained in this way without invoking a sustained source  
427 mechanism (Azpiroz-Zabala et al., 2017). The timescale of duration of turbidity currents at a location  
428 can thus be estimated by dividing the distance to the source area by a characteristic stretching-  
429 velocity scale of the currents. The estimation of the stretching velocity scale might require an  
430 iterative procedure where the SBE is initially used to reconstruct velocity profiles, which are  
431 subsequently used to evaluate the turbidity current duration boundary condition for sediment  
432 budget estimations. An alternative workflow in ancient and subsurface cases, where uncertainties  
433 are inherently large, might be to set broad ranges of turbidity current durations based on the  
434 geological setting (Table 1): minutes to 1 hour for delta slopes; hours to 10 hours for canyons in the  
435 upper continental slope and slope channels in smaller basins with steep slopes; 10 hours to a few  
436 days for larger canyons in the lower continental slope; and a few days to a week for distal parts of  
437 large (~1000 km long) submarine fans.

438

439 **Recurrence Time** --- Recurrence times of turbidity currents are increasingly well constrained  
440 in literature (Piper & Deptuck, 1997; Pirmez & Imran, 2003; Xu, 2011; Talling *et al.*, 2013; Clare *et al.*,  
441 2014, 2016; Stevens *et al.*, 2014; Azpiroz-Zabala *et al.*, 2017; Allin *et al.*, 2018; Jobe *et al.*, 2018;  
442 Stacey *et al.*, 2019). Much direct monitoring evidence points to a few to many tens of turbidity  
443 currents being generated each year at the top of the slope in active systems. This activity can be  
444 bundled seasonally in summer in response to meltwater hydrographs (Clare *et al.*, 2016; Hizzett *et*  
445 *al.*, 2018), or winter in response to storm activity (Xu *et al.*, 2004; Pope *et al.*, 2017). These very short  
446 recurrence times rapidly increase down-slope (Stevens *et al.*, 2014; Allin *et al.*, 2018; Stacey *et al.*,  
447 2019), because many turbidity currents dissipate within the slope system (Heerema *et al.*, 2020),  
448 which is thus a staging area for sediment that is only occasionally exported all the way to the basin  
449 floor by large, fan-building turbidity currents (Jobe *et al.*, 2018; Heijnen et al., 2022). Recurrence time

450 of turbidity currents thus depends highly on the position in the system of interest, the mechanism  
451 that ignites these flows, and the size of the shelf itself. Consequently, flow frequency can vary from  
452 weekly to monthly or seasonal event in low storage capacity (short) shelves, to decadal, centennial,  
453 or even millennial -scale recurrence intervals in high storage capacity (broad) shelves, especially if  
454 these flows are triggered through geologic factors like the Grand Banks earthquake rather than  
455 fluvial flooding as per the Congo system. In summary (Table 1), if upper slope sedimentation is of  
456 most interest, the shorter recurrence times are advised as input. If sediment export to submarine  
457 fans at the base of slope is of interest, recurrence times of decades to centuries can be appropriate  
458 (see Jobe et al., 2018, for compilations of recurrence times in dated Quaternary fan systems), though  
459 evidence suggests that turbidity currents travel down major channel-levee systems, such as the  
460 Amazon, annually during periods of glacioeustatic lowstands of sea level (Piper & Deptuck, 1997;  
461 Pirmez & Imran, 2003). The largest millennial recurrence times seem to be restricted to abyssal-plain  
462 settings and systems where turbidity currents are triggered by rare seismic events (Clare *et al.*, 2014).  
463 If recurrence times for ancient examples are considered too uncertain to set as an input condition, an  
464 alternative strategy is to enforce an event count, based on stratigraphic evidence, by the  
465 combination of recurrence time and duration of system activity.

466

467 **Allocyclic System Activity** --- The duration and recurrence time of turbidity currents are both  
468 aspects of the short timescale punctuation of submarine channel activity. Punctuation of activity also  
469 exists on longer timescales. This long timescale punctuation of activity generally relates to external,  
470 or allogenic, forcing that causes periodic attachment and detachment from the feeder systems of the  
471 submarine depositional system (e.g. shelf-edge deltas; littoral cells; or estuaries). The SBE should  
472 primarily be used to determine the sediment budget for these active phases of sediment delivery in  
473 deep marine systems.

474 A classic concept from sequence stratigraphy assumes deep water activity in sedimentary systems is  
475 highest during relative-sea-level lowstands (e.g. Posamentier and Vail, 1988). This concept has been

476 validated on various deep-water systems around the world, especially for the Pleistocene era  
477 (Anderson, 2016; Sylvester, 2012). The lowstand-activity concept is most appropriate for non-  
478 glaciated, tectonically passive margins in ice-house worlds. In such lowstand-dominated systems, the  
479 deep-water system activity duration should be set by the user to the phase within the relative sea  
480 level cycle during which shelf-edge deltas are present (Falivene et al., 2020). For example, Pirmez et  
481 al. (2012) document that sedimentation in the Brazos-Trinity system in the Gulf of Mexico took place  
482 mostly in the 9 kyr period from 24-15 ka, around the maximum sea-level lowstand in the latest Late  
483 Glacial Maximum. In the case of the Niger Delta system, Jobe et al. (2015) documented how  
484 lowstand activity lasted ~30-35 kyr within a ~100 kyr glacioeustatic cycle.

485 The effect of sea-level fluctuations on deep water sediment delivery can be fundamentally different  
486 in steep, tectonically active systems characterized by a narrow shelf (Covault *et al.*, 2007). Covault et  
487 al. (2007) documented how sediment derived from part of Southern California is predominantly  
488 delivered to submarine fans during sea level highstand, when the Oceanside littoral cell is at its peak  
489 activity and generates a high supply of sediment to the la Jolla Canyon head. The Congo Canyon  
490 system is another example that does not follow the sea-level lowstand paradigm (Khipounoff *et al.*,  
491 2003; Azpiroz-Zabala *et al.*, 2017) due to the direct connection that exists between the Congo Canyon  
492 head and the Congo Estuary. These examples illustrate that strict application of a low-stand activity  
493 paradigm should be avoided if particular aspects of the basin configuration invalidate them.

494 Many deep-water depositional systems of interest were active in Jurassic, Cretaceous, or Paleogene  
495 times, when fluctuations of relative sea-level are generally believed to have been less prominent as a  
496 forcing of sediment supply to deep-water depositional systems (Blum and Hattier-Womack, 2009). In  
497 such systems climate forcing is operating through mechanisms other than glacio-eustacy, for instance  
498 by forcing sediment production and transport cycles on the continents (Carvajal and Steel, 2006;  
499 Zhang et al., 2019). Interestingly, the time scale of these climatic forcing of sediment supply appears  
500 to be of order 10-100 kyr, which is similar to the glacio-eustatic lowstand re-occurrence times  
501 discussed above (Carvajal and Steel, 2006; Crabaugh and Steel, 2004; Grundvåg et al., 2014; Burgess

502 and Hovius, 1998; Blum & Hattier-Womack, 2009). In such cases the system activity parameter of the  
503 SBE should be set to the length of time within the climatic cycle that characterizes the phase of  
504 maximum regression of deltas to the basin margin.

505

506

### 507 **SBE-RESULT STRUCTURE AND SENSITIVITY ANALYSIS**

508 The structure of the default SBE results is illustrated with a simulation of a hypothetical system (see  
509 Table 2 for an overview of conditions). Figure 3 displays the default results of the SBE run with these  
510 input conditions. The velocity and concentration profiles of all simulated turbidity currents are stored  
511 by the SBE, but for simplicity only the profiles of a single simulated turbidity current are displayed as  
512 an example (Fig. 3a&b). This example simulation is picked from the characteristic turbidity currents  
513 whose maximum velocity is closest to the mean of all simulated maximum velocities.

514 The turbidity currents in this hypothetical system have a maximum velocity of  $\sim 3$  m/s, are highly  
515 stratified with a maximum concentration near the bed of  $\sim 6\%$ , transport  $\sim 15$  m<sup>3</sup> of sediment every  
516 second, which amounts to  $\sim 0.1$  km<sup>3</sup> of sediment per cycle (Fig. 3). These results serve as the reference  
517 to a) explore the sensitivity of the simulation results to uncertainty of the input conditions, and b) the  
518 response of the results to changing input conditions.

519

520 The sensitivity of the SBE to changes in input conditions is tested by reducing the uncertainty of all  
521 input variables, apart from one, to  $\pm 1\%$  of the mean of the base case input range. The simulation is  
522 repeated with the uncertainty of a single different variable reinstated each time. The sediment  
523 budgets of all the simulations are displayed in order of descending spread of the predicted sediment  
524 budgets (Fig. 4), in a tornado diagram (Holbrook & Wanas 2014; Lin & Battacharya 2017). These  
525 diagrams reflect the sensitivity of the model output to the uncertainty of the variables used as input  
526 conditions. The average input sediment concentration comes out as the variable with most impact on  
527 the simulation results (Fig. 4a); most of the spread of the base case is maintained when all variables

528 apart from the sediment concentration are set to range +/-1% around the mean of the base case  
529 input. Channel width also has a relatively large impact on the spread of the sediment budget results,  
530 but is a distant second to the sediment concentration parameter. The three temporal parameters in  
531 the SBE (flow duration, frequency and system activity) show an identical and moderate influence on  
532 the spread of the sediment budget. Channel depth, interestingly has a smaller impact on the total  
533 uncertainty. The insensitivity to uncertainty in slope of the system is striking: the spread of predicted  
534 sediment budgets is reduced to a narrow range while the slope is still varied from 1° to 2.5° (Fig. 4a).  
535 There is thus very little benefit to be gained from increasing the confidence levels of slope estimates.  
536 This is a somewhat unexpected result due to the importance generally attributed to slope in the  
537 literature (Kneller, 2003; Stevenson *et al.*, 2015; Pohl *et al.*, 2020).  
538 Achieving uncertainty levels of +/-1% is unrealistic in natural turbidity current systems. Another  
539 tornado diagram is therefore produced for which uncertainties in all variables apart from one have  
540 been reduced by 50% (Fig. 4b). This diagram confirms the sensitivity ranking of variables that was  
541 found in Fig. 4a. It also shows that the spread in sediment budgets in most simulations is rather equal  
542 to that of the simulation where uncertainty in all variables has been reduced by 50% (Fig. 4b). This  
543 result indicates that it is acceptable for relatively high uncertainty to remain in one or two of the  
544 intermediate-sensitivity input parameters. There is little benefit in spending much effort on reducing  
545 that uncertainty of a single variable, because the spread in sediment budgets will remain similar even  
546 if its uncertainty is reduced by 50%. The exception to this is the input sediment concentration: even if  
547 all other variables are set to a 50% reduction of uncertainty, the spread of results does not decrease  
548 much (Fig. 4b), which again points to the importance of uncertainty about sediment concentration in  
549 turbidity currents.

550 As a final exercise in this section, the base case is repeated with the input range doubled for one  
551 variable at a time. The duration, frequency, and system activity all have a linear relation with the  
552 sediment budget, and doubling these variables results in doubling of the simulated sediment budgets  
553 (Fig. 4c). Channel width and sediment concentration both have a nonlinear effect. The concentration

554 again has the largest impact with the predicted sediment budgets quadrupling as a result of the  
555 doubled input range. Channel depth has a subdued effect, and doubling of the slope range from 1-  
556 2.5° to 2-5°, a dramatic increase in slope within the band-width of natural slope angles, merely has  
557 the effect of increasing the spread of predicted sediment budgets somewhat.

558

559

## VALIDATION OF THE MODEL

560 We validate the SBE app here with examples of the smallest and largest scale turbidity currents on  
561 earth for which detailed data is available: laboratory turbidity currents and the 1929 Grand Banks  
562 turbidity current.

563

564

### *Laboratory Turbidity Currents*

565

566

567

568

569

570

571

572

573

574

575

576

577

578

579

**Boundary Conditions** --- The model is first tested on Run 3 of de Leeuw et al. (2018b). This experiment was selected because it displayed the least amount of in-channel and levee deposition of all the experiments reported in that paper. It was therefore most representative of a bypassing channel, indicative of the flow-channel size equilibrium discussed in section 2.3, above. The size of the pre-formed channel did result in a phase of initial channel deepening and widening (Fig. 5a), which indicates that the initial channel dimensions were smaller than the dimensions in equilibrium with the characteristic turbidity current initiated by de Leeuw et al. (2018b). The velocimetry data shows that channel deepening took place in the initial 40 seconds of the experiment, after which the channel thalweg stays at a constant elevation throughout the final 40 seconds of the experiment (Fig. 5b). This is interpreted here to indicate that the initial erosive channel enlargement led to an equilibrium between the turbidity current and the channel dimensions. The channel dimensions used as input for the SBE are therefore obtained from the digital elevation model of the topography measured after the experiment. The input sediment concentration of the experiment has been reported as 17% (de Leeuw et al., 2018b). The importance of the sediment concentration in the sensitivity analysis led to a reevaluation of this experimental parameter. Scrutiny of the laboratory

580 logbook of the experiment revealed that the volume of water supplied to the mixing tank could have  
581 been as much as 0.928 m<sup>3</sup>, and that 28 kg of sediment has been recorded to remain in the pump &  
582 pipe system that supplies the mixture to the Eurotank. While the sediment in the pipes lowers the  
583 experimental sediment budget slightly, in combination with the elevated water volume it implies that  
584 the actual experimental sediment concentration could have been as low as 15% instead of the  
585 intended 17%. The full list of input conditions for the SBE are displayed in Table 2. The uncertainty  
586 ranges for the input conditions have been determined by applying an error margin of +/-10% to the  
587 best guess values, which is appropriate for controlled sedimentology experiments.

588         **Results** --- The SBE overestimated the velocity of the experimental turbidity current; the  
589 mean of predicted velocity maxima is 50% larger than the measured velocity maximum (Fig. 6a; 2.0  
590 m/s vs 1.36 m/s). The predicted concentration profile has elevated concentrations near the base and  
591 decreased concentrations towards the top compared to the average input concentration (Fig. 6b).  
592 The predicted basal sediment concentration reaches the maximum granular concentration due to the  
593 high bed shear stress. The concentration profile was not measured by de Leeuw et al. (2018b), but  
594 concentrations obtained by siphoning similar turbidity currents in another set-up suggest that basal  
595 sediment concentrations reach ~30% (e.g. Pohl et al., 2020), not the 50+% predicted by the SBE. The  
596 experimental sediment budget falls below the range of predicted values (Fig. 6c&d). The minimum of  
597 predicted budgets is 32% higher than the experimental value; and the p<sub>50</sub> of predicted budgets is a  
598 factor 2.9 times the amount of sediment pumped into the experiment.

599         **Evaluation** --- Approximately half of the predicted sediment budgets falls within a factor of 2-  
600 3 of the amount of sediment pumped into the experiment. This is the expected level of accuracy of  
601 any sediment-flux estimations obtained from comparatively simple and tightly controlled open-  
602 channel flows (Chang, 1988). Yet the discrepancy invites scrutiny.

603         Despite the experiment being well-controlled, the evolution of channel-shape is rather  
604 intricate due to a combination of levee aggradation, channel-thalweg incision, and channel-margin  
605 erosion occurring (de Leeuw et al., 2018b). The over-predicted velocity and concentration profiles



606 may suggest that the final phase of the experiment represents an entrenched state of a turbidity  
607 current in a channel that is in equilibrium with a stronger current. This consideration is tested by  
608 broadening the range of channel morphologies to that of the other experiments of de Leeuw et al.  
609 (2018b) that were found to be more or less in equilibrium with the input conditions (Table 2). This  
610 increased uncertainty in representative channel shapes improves the fit between experiment and  
611 predictions. The weakest predicted velocity profile is now similar to the measured velocity profile  
612 (Fig. 6e), a considerable improvement over the narrowly-constrained predictions (Fig. 6a).

613 Another major contributor to the original discrepancy between experiment and prediction  
614 could be the eroded sediment added to the turbidity current in excess of the budget supplied from  
615 the mixing tank, which is estimated to be ~60 liters (an average of 3 cm erosion over a 0.8 m wide 4  
616 m long channel section). Addition of this eroded sediment to the sediment budget raises it to ~0.20  
617 m<sup>3</sup>, the p<sub>26</sub> value of the simulated population (Fig. 6f).

618 The increased uncertainty improves the match between experiment and prediction.  
619 Increased precision in boundary conditions may lead to more specific results, yet such specificity  
620 should not be mistaken for increased accuracy.

621

#### 622 *Validation against the 1929 Grand Banks turbidity current*

623 **Boundary Conditions** --- The 1929 Grand Banks turbidity current is the largest scale event, in  
624 terms of volume of sediment transported, for which data on bathymetry, flow velocity, flow  
625 thickness, and flow composition is available (Heezen & Ewing, 1952; Piper & Aksu, 1987; Piper *et al.*,  
626 1988; Hughes Clark *et al.*, 1990; Krastel *et al.*, 2016; Stevenson *et al.*, 2018). It has long been used as  
627 a testing ground for models of turbidity current dynamics (Kuenen, 1952; Plapp & Mitchell, 1960;  
628 Stevenson *et al.*, 2018). Insights from the 2015 RV Maria S. Merian cruise (Cruise No. MSM47; Krastel  
629 *et al.*, 2016; Stevenson *et al.*, 2018) are used here to constrain the SBE (Table 2). The aim of this  
630 exercise is to validate the velocity and concentration results of the SBE and establish how the range  
631 of sediment budget estimates from the SBE relates to the estimated volume of 175-185 km<sup>3</sup> of the

632 deposit that was formed on the Atlantic abyssal plane during this event (Piper & Aksu, 1987; Piper *et*  
633 *al.*, 1988). Specific focus is put on Transect 2 of the Eastern Valley (Stevenson *et al.*, 2018).  
634 Approximately 70 km<sup>3</sup> of sediment (excluding deposit porosity; see Stevenson *et al.*, 2018) passed  
635 through this section. The rest of the sediment forming the 175-185 km<sup>3</sup> deposit on the abyssal plane  
636 was transported along other flow-pathways on the Grand Banks continental slope.  
637 The boundary conditions for the simulation of the Grand Banks turbidity current are set using a  
638 combination of parameters measured in the field and reconstructed flow properties such as  
639 sediment concentration (from Stevenson *et al.*, 2018). Channel bathymetry at Transect 2 across the  
640 Eastern Valley provides constraints on flow thickness (201 m), channel width (23,000 m) and slope  
641 (0.45°). Cable breaks across this part of the slope measured the flow speed to be 19.1 m/s (Heezen &  
642 Ewing, 1952). From these data the depth-averaged sediment concentration of the flow was  
643 reconstructed between 2.7-5.4 % by volume (Stevenson *et al.*, 2018).

644

645 **Results** --- The SBE model shows remarkable agreement with the observed and  
646 reconstructed properties of the 1929 Grand Banks deposit and flow (Fig. 7). The velocity profile of a  
647 representative simulated flow shows a velocity maximum being slightly higher than 20 m/s, which is  
648 consistent with the velocity of 19 m/s deduced from the timing of cable breaks (Fig. 7a). The  
649 concentration profile indicates a highly stratified dense basal flow with high concentrations (>10%)  
650 up to ~25m from the bed, overlain by a low-density cloud (Fig. 7b).  
651 The predicted sediment flux through the channel at Transect 2 was  $\sim 3 \cdot 10^6$  m<sup>3</sup>/s ( $p_{50}$ ; Fig. 7c), an  
652 order of magnitude more than the water discharge of the Amazon, which is largest river on Earth by  
653 discharge. This flux is combined with an estimated 4-8 hour flow duration (Stevenson *et al.*, 2018).  
654 The model then predicts a  $p_{50}$  of sediment volume of 60 km<sup>3</sup> with a  $p_{10}$ - $p_{90}$  range between ~30 and  
655 ~100 km<sup>3</sup> (Fig. 7d).

656 **Evaluation** --- The input sediment concentration used had a broad range from 2.7-5.4%, and  
657 it was shown in the general sensitivity analysis that this can impact the SBE results to a great extent

658 (Fig. 4). To explore the validity of these results we first present a sensitivity analysis on the sediment  
659 concentration parameter. Simulations were repeated with all parameters except the concentration  
660 kept the same; the concentration range was adjusted to the lower end and upper end of the  
661 estimates by Stevenson et al. (2018), each with a +/-10% uncertainty (Table 2). Low sediment  
662 concentrations of 2.7% result in flow velocities of ~15m/s (Fig. 8). In contrast, using a high sediment  
663 concentration condition of 4.9-5.9% results in flow velocities of ~23 m/s. The low and high end of  
664 Stevenson et al.'s (2018) concentration reconstructions thus result in under- and over-estimation of  
665 the Grand Banks velocity respectively. A concentration value midway between 2.7 and 5.4% (~4 %)  
666 produces flow velocities very similar to the values measured in the field (Fig. 7b). At the same time  
667 this result validates the velocity function of the SBE and the sediment concentration reconstruction  
668 by Stevenson et al. (2018). It is worthwhile emphasizing that the sediment concentration range was  
669 estimated by Stevenson et al. (2018) based on Chézy friction equations. This Chézy calculation output  
670 is used as an input constraint in the SBE simulation. The success of the present analysis should  
671 therefore not be seen as an independent validation against measurements only. Rather, the SBE is a  
672 corroboration of Chézy approaches (Middleton, 1966; Zeng *et al.*, 1991; Konsoer *et al.*, 2013;  
673 Stevenson *et al.*, 2018; Simmons *et al.*, 2020), while modelling the effects of the mixing layer through  
674 a technique rooted in fluid mechanics (Pope, 2000) rather than empirical coefficients. Stevenson et  
675 al.'s (2018) estimated flow duration of 4-8 hours was used in the SBE Grand Banks simulation (Table  
676 2). The range of calculated sediment budgets is centered around the 70 km<sup>3</sup> observed in the field.  
677 Though this result seems remarkable it adds little to the validation of the velocity and concentration  
678 scales because the SBE procedure is simply the inverse of the duration calculations performed by  
679 Stevenson et al. (2018): they estimated flow duration by dividing the sediment budget transported  
680 through the Eastern Valley by average velocity and concentration. It does illustrate, however, how  
681 the SBE quantifies the effects of remaining geologic uncertainties explicitly by reconstructing a  
682 histogram of likely sediment budgets, with a p<sub>10</sub>-p<sub>90</sub> range of 30-100 km<sup>3</sup>, centered on the remarkable

683 volume of 70 km<sup>3</sup> sediment transported through Transect 2 of the Eastern Valley during the Grand  
684 Banks event (Piper et al., 1988; Stevenson et al., 2018).

685

686 *Validation discussion: The smallest and the largest.*

687 Heezen and Ewing (1952), and Kuenen (1952) perceived the recording of the 1929 Grand Banks event  
688 by cable breaks as a turbidity current experiment at the largest scale possible on Earth. The Eurotank  
689 experiments represent the smallest scale at which turbidity currents can be studied with natural  
690 sediments, a fluid with the viscosity of water at room temperature, and with a gravitational  
691 acceleration of 1\*g. The SBE performs within standard acceptable accuracy of sediment flux  
692 predictors in these validations in isolation. It is remarkable that the SBE achieves this level of success  
693 at the smallest and largest scales possible on planet Earth, which are separated by 12 orders of  
694 magnitude, without any changes in parameterizations or the equations themselves. There is  
695 apparently no application on Earth that is outside the range of scales for the SBE, and no need to  
696 apply it outside the range for which it is established. This robustness of the SBE encourages us to  
697 seek applications of the SBE in cases where it is predictive without the possibility of validation.

698

#### 699 **APPLICATION OF THE SBE TO AN ANCIENT CHANNEL DEPOSIT IN OUTCROP**

700 The slope channels of the Cretaceous Tres Pasos Formation (Chile) have been extensively studied in  
701 the past decade (e.g. Hubbard et al., 2010; Macauley and Hubbard, 2013; Hubbard et al., 2014;  
702 Pemberton et al., 2016; Reimchen et al., 2016; Daniels et al., 2018; Hubbard et al., 2020) and provide  
703 an excellent testing ground for the application of the SBE to an ancient deep-water depositional  
704 system. One of the challenges of applying the SBE to ancient systems is making the distinction  
705 between the dimensions of channel fill deposits and the dimensions of the conduits for the  
706 characteristic turbidity currents. Channel fill sandstones are commonly compound deposits formed  
707 by multiple turbidity currents during alternating phases of erosion and deposition. Thus channel  
708 dimensions associated with a single turbidity current are not the same as those of the channel fills.

709 Hubbard et al (2014; 2020) recognized this discrepancy and argued for using inter-channel erosion  
710 surfaces to make the distinction between sediment conduit dimensions (“storey” deposit) versus  
711 those of the composite channel element. The analysis below will investigate the significance of this  
712 interpretation for the projected sediment budget associated with the lifespan of a channel element.  
713 Additionally, an erroneous attribution of channel complex dimensions, which are commonly  
714 observed in seismic data (Samuel et al., 2003; Macauley & Hubbard, 2013), to the characteristic  
715 turbidity current scale will be investigated.

716

### 717 *Boundary Conditions*

718 **Channel form dimensions** --- Channel form dimensions are estimated for the “M2” channel  
719 element, which is the focus of the recent paper by Hubbard et al. (2020). Three sets of dimensions  
720 are used as input conditions (Table 3): a) intra-channel element surfaces delineating channel storey  
721 deposits have vertical and horizontal scales of 2.5-6.5 m and ~200 m, respectively (Hubbard et al.,  
722 2020); b) the primary channel surface delineating the M2 channel element deposit has a vertical  
723 scale of 17 m, and is estimated to be 400 m wide (Hubbard et al., 202X); and c) channel elements are  
724 commonly grouped in channel complexes that are typically 800-1000 m wide, and 30-60 m thick  
725 (Macauley and Hubbard, 2013).

726 **System Slope** --- The M2 channel is part of the Figueroa clinothem (*sensu* Hubbard et al.,  
727 2010), which has an estimated paleorelief of ~1000 m. Daniels et al. (2018) estimated the paleo-slope  
728 at this position in the Figueroa clinothem at 0.7-0.9°.

729 **Grainsize** --- The axial channel-fill deposits of the Tres Pasos Formation slope channels are  
730 dominated by amalgamated, thick bedded, fine to medium-grained sandstones. Grainsize  
731 measurements on thin section images yielded a  $D_{50}$  of 200  $\mu\text{m}$  (de Leeuw, 2017). The  $D_{90}$  was  
732 measured as 400  $\mu\text{m}$ .

733 **Turbidity current duration** --- Tres Pasos Formation contains relatively small, slope channels  
734 with a length of 10s of km, and the flow duration is therefore set to 3-6 hours.



760 km<sup>3</sup> (p<sub>10</sub>-p<sub>50</sub>-p<sub>90</sub>) over the full evolution of the 500 turbidity currents that formed the channel-  
761 element deposit (Fig. 9d).

762 **Storey – element – complex** --- The larger dimensions of the composite channel-element and  
763 channel-complex scales lead, if associated with characteristic turbidity currents, to much larger flows  
764 and sediment budgets (Fig. 10). The simulated flow velocities increase to 2.5 and 4 m/s, respectively  
765 (Fig. 10a). This combines with the much thicker column of suspended sediment to accumulate  
766 sediment budgets that are in the order of 0.1 km<sup>3</sup> for the element-dimension simulations and 1 km<sup>3</sup>  
767 for the complex-dimensions simulations, compared to 0.01 km<sup>3</sup> simulated when storey dimensions  
768 are used to simulate the characteristic turbidity currents (Fig. 10b).

769

770 *Discussion of application to an ancient example*

771 **Highly stratified turbidity current structure** --- The majority of the sediment in the  
772 characteristic turbidity currents simulated for the Tres Pasos Formation M2 channel is suspended  
773 near the base of the flow. The remainder of what would typically be viewed as “the turbidity current”  
774 (say from 2-12 m above the bed), is relatively devoid of sediment. This result corroborates recently  
775 emerging measurements and perspectives on the concentration structure of turbidity currents.  
776 Measurements of sediment concentration with Acoustic Doppler Current Profilers (ADCPs) indicate  
777 that sediment concentrations in the bulk of the recorded flows are indeed very low (~0.02 %;  
778 Azpiroz-Zabala et al., 2017; Simmons et al., 2020). ADCPs have generally been deployed above  
779 submarine channels and canyons, to monitor turbidity currents downwards, which gives interference  
780 and resolution problems near the bed. These measurement difficulties mean that the 2 m thick part  
781 with elevated sediment concentrations depicted in Fig. 9b would typically be poorly resolved at most  
782 in ADCP data (Simmons et al., 2020). This would obscure the fact that the turbidity current is a very  
783 dilute cloud that is driven mainly by a dense basal layer (Cartigny et al., 2013; Paull et al., 2018;  
784 Simmons et al., 2020).

785 It is interesting to discuss here how stratification of concentration profiles is included in depth-  
786 averaged modelling workflows of turbidity currents, an approach that is more complicated than the  
787 simplified approach of the SBE. Parker (1982) proposed a simple measure for stratification in depth-  
788 averaged modelling of turbidity currents: the ratio between the near-bed sediment concentration  
789 and the depth-averaged sediment concentration,  $r_o$ , a notation that has mostly been followed by the  
790 many papers following the depth-averaged approach to modelling turbidity currents (for recent  
791 examples see Halsey et al., 2017; Bolla Pittaluga et al., 2018; Traer et al., 2018). On its first  
792 appearance,  $r_o$  was evaluated as a function of grain size with the Rouse equation for suspended  
793 sediment concentration (Parker, 1982). The Rouse equation was not derived for turbidity currents,  
794 but for open channel flow (Rouse, 1937). Even though it has been shown to be a reasonable  
795 approximation for fine grained suspended sand, and in general for the sediment suspended in the  
796 lower part of the flow, it mispredicts suspension of mud, especially in the upper part of the flow,  
797 because it neglects mixing with the ambient water in the mixing layer (Jobe et al., 2017; Eggenhuisen  
798 et al., 2019). Parker et al. (1986) dropped reliance on the Rouse equation and instead advised a value  
799 of  $r_o=1.6$ , while Garcia (1994) advised  $r_o=2.0$ , both based on a compilation of concentration profiles  
800 obtained from weakly-stratified, small-scale laboratory experiments. These low values for  $r_o$  are used  
801 in modelling studies to this date (Traer et al., 2012; Halsey et al., 2017; Bolla Pittaluga et al., 2018).  
802 Dorrell et al. (2014) attempted to validate depth-averaged simulations with unstratified “top-hat”  
803 concentration profiles (with  $r_o=1$ ) and weakly-stratified profiles against measurements of gravity  
804 currents in the Black Sea. The unsatisfactory results of their validation led Dorrell et al. (2014) to  
805 hypothesize that field-scale flows have larger degrees of stratification that are poorly represented by  
806 the stratification observed in small scale experiments. Recent acoustic measurements of sediment  
807 concentrations in the Congo Canyon indicate that  $r_o$  was  $\sim 10$  in the turbidity currents reported by  
808 Azpiroz-Zabala et al. (2017) and Simmons et al. (2020). The SBE results presented here are consistent  
809 with this elevated stratification in field-scale turbidity currents compared to laboratory turbidity



810 currents, with  $r_o \sim 10$  for the Tres Pasos simulations (Fig. 7b), and  $r_o \sim 11$  for the Grand Banks simulation  
811 (Fig. 9b).

812

813 **Sediment flux and budget of the M2 channel element** --- The simulated sediment flux  
814 through the M2 channel (Fig. 9) is comparable to the sediment flux of the turbidity currents in the  
815 Congo Canyon reported by Azpiroz-Zabala et al. (2017). The total sediment budget of the M2 channel  
816 element is comparable to the “X-channel” on the Niger slope (0.02-0.05 km<sup>3</sup>; Jobe et al., 2018),  
817 though this was delivered to the lobe by a smaller number (20-50) of turbidity currents with a  
818 centennial recurrence time, rather than the 500 events of the M2 channel. The M2 sediment budget  
819 is smaller than the volumes of other Quaternary fans evaluated in Jobe et al. (2018), which are  
820 typically order 1 km<sup>3</sup> with event counts varying from 10-700. This comparison shows that the  
821 reconstructed sediment flux and budget for the M2 channel are within the bandwidth of values  
822 measured in other systems, though on the lower part of this bandwidth. This is consistent with the  
823 suggestion by Jobe et al (2018) that smaller volumes are associated with intraslope and base-of-slope  
824 channels. A consideration of stratigraphic hierarchy could also explain the modest sediment budget  
825 predicted for the M2 channel element. Though it is not entirely clear whether lobe elements (Prélat  
826 *et al.*, 2009) can be correlated one-to-one with a single, coeval channel element (Cullis *et al.*, 2018), it  
827 is interesting to observe that the predicted sediment budget for the M2 channel compares very well  
828 with the volume estimates of lobe elements compiled by Prélat et al. (2010). This point will be  
829 considered further in the section below.

830

831 **Storey – Element – Complex – Fan** --- Constraining the SBE with different hierarchical scales  
832 leads to disparate distributions of predicted sediment budgets (Fig. 10): the ranges of the 3 sets of  
833 predicted sediment budgets do not overlap. Each step upward in dimensions of the assumed  
834 contemporaneous channel form results in roughly an order of magnitude increase in predicted  
835 sediment budget. Hubbard et al. (2014; 2020) have argued extensively for associating intra channel-

836 element surfaces to the scale of formative turbidity current processes based on facies analyses. The  
837 larger channel-fill deposits recognized in single channel elements are formed by a compound  
838 evolution of erosion and deposition, akin to “the fluvial valleys that never were” of Strong and Paola  
839 (2008; Hubbard et al., 2020). Association of channel element thickness with formative turbidity  
840 current flows would lead to much thicker (17 m vs 2.5-6.5 m; Fig. 10a) and faster flow (~2.5 m/s vs.  
841 ~1 m/s; Fig. 10a), which combines to yield an order of magnitude larger sediment budget over the  
842 lifespan of the M2 element (Fig. 10b).

843 Multiple channel elements are commonly stacked consistently into channel complexes (e.g.  
844 McHargue et al., 2011; Macauley and Hubbard, 2013). In our preferred interpretation, the sediment  
845 budget for channel complexes is obtained by multiplying the budget based on intra-channel surfaces  
846 (channel storey dimensions) by the typical count of elements in a complex rather than using channel-  
847 complex dimensions as inputs to SBE. Macauley and Hubbard (2013) mapped 18 channel elements in  
848 the three channel complexes that form the lower half of the Figueroa clinothem. This suggests a  
849 typical sediment budget during one channel complex evolution of  $\sim 0.1 \text{ km}^3$  ( $p_{50}$ ), much less than the  
850 volumes predicted if the complex dimensions were erroneously associated with formative turbidity  
851 currents ( $p_{50} = 1 \text{ km}^3$ ; Fig. 10b). A similar point is made by Covault et al. (2021) who emphasise the  
852 difference in scale between the “characteristic channel width” and the much larger channelbelt  
853 width in high-sinuosity meandering submarine channels. This illustrates the consequences of  
854 erroneously relating channel fill, channel complex, or channelbelt dimensions to the sizes of their  
855 formative flows. It also emphasizes that careful interpretation of stratigraphy is critical for accurate  
856 estimation of primary aspects of the system, such as the order of magnitude of sand transported  
857 down-dip. This is particularly important in large-scale subsurface datasets that can lack resolution to  
858 map individual elements.

859 Extrapolation of the sediment budget to the entire sand-rich package of the Figueroa clinothem at  
860 the Laguna Figueroa localities (Macauley and Hubbard, 2013; Hubbard et al., 2014; Pemberton et al.,  
861 2016; Hubbard et al., 2020) yields a total SBE-derived turbidity-current sediment budget of order 1

862 km<sup>3</sup>. This volume would have been deposited during an unconstrained subsidiary phase within an ~ 2  
863 Myr stratigraphic interval duration (Daniels et al., 2018). The depositional body formed at this largest  
864 timescale could appropriately be called a fan. This SBE volume estimate is an entry into the suite of  
865 source-to-sink metric correlations available from literature (Sømme *et al.*, 2009a; 2009b). A 1 km<sup>3</sup>  
866 sediment volume for the Figueroa clinothem fan could correlate to a fan length of 20-150 km, and a  
867 fan area of order 1000 km<sup>2</sup> (Sømme *et al.*, 2009b).

868

869

## GENERAL DISCUSSION

870

871

### *An Extra Tool in the Source-to-Sink Toolshed*

872 Estimations of sediment budgets in submarine depositional systems can also form an inroad into a  
873 broader understanding of the setting of the system in a source-to-sink analysis (Jobe et al., 2018). An  
874 important aspect of source-to-sink analyses is that metrics obtained for different segments can be  
875 correlated to each other because regional plate tectonic and climatic conditions ensure regulate  
876 consistency within a system (Sømme *et al.*, 2009b; a; Walsh *et al.*, 2016). By predicting metrics of  
877 basin-floor lobes from base-of-slope channel metrics the SBE intrinsically correlates between the  
878 deep-marine segments of the chain of sediment transport. Furthermore, the reconstructed fan  
879 volume, length, and area can be used to estimate slope length (Sømme *et al.*, 2009a; 2009b). The  
880 estimated slope length for the Tres Pasos Formation example analysed above would be kilometers to  
881 tens of kilometers, which is consistent with the stratigraphic reconstructions of Daniels et al. (2018).  
882 Dimensions of the shelf-staging area (Sømme et al., 2009a) can be evaluated against the depositional  
883 style of coeval shelf-top delta deposits of the Dorotea Formation (Romans *et al.*, 2011; Daniels *et al.*,  
884 2018). And correlated long-term deposition rates of order 10<sup>6</sup> t/yr (Sømme *et al.*, 2009a) can be used  
885 to evaluate the nature of river catchment areas that supplied sediment from the Andes into the  
886 retro-arc foreland basin (Romans *et al.*, 2011).

887 Sediment budget estimations are a rapidly evolving topic in sedimentary system science. It has been  
888 developed for the sediment budget coming from continental catchment areas over decadal  
889 timescales in the BQART model (Syvitsky & Milliman, 2007; Sømme *et al.*, 2011; Helland-hansen *et*  
890 *al.*, 2016), and for the geological sediment budget in fluvial systems using the fulcrum approach  
891 (Holbrook & Wanas, 2014; Bhattacharya *et al.*, 2016; Lin & Bhattacharya, 2017; Sharma *et al.*, 2017).  
892 Estimations with as many different tools as possible are combined in an ideal source-to-sink study.  
893 Where possible, triple assessments with BQART on catchment area budget, the fulcrum approach for  
894 the fluvial segment, and the SBE for the deep-marine segments will result in a consistency check that  
895 can confirm the source-to-sink understanding of a system.

896

#### 897 *Model functionality and complexity*

898 **Functionality** --- The SBE is an example of simplified modelling where much of the hydraulic  
899 complexity is hidden from the intended users (marine and sedimentary geologists) because it could  
900 lie outside their immediate area of expertise. The simplicity of the model presented here allows  
901 computation of  $10^4$  turbidity currents within seconds on a standard computer. This makes the tool  
902 suited to consider multitudes of scenarios, resulting in the probability distribution function of  
903 sediment fluxes into the deep oceans. Also, its computational efficiency lends itself to running  
904 multiple simulations to test different geological perspectives, and the overall sensitivity of the  
905 system. The benefit of such a rapid interaction is that the geologist gains immediate insight into the  
906 consequence of different geological models for the probability distribution of predicted sediment  
907 budgets. The Tres Pasos Formation evaluation shows that interpretations of stratigraphic hierarchy  
908 are a primary control on the scale of sediment budget estimations. An even more fundamental point  
909 is made here by comparing budget histograms of simulations with different uncertainty bounds  
910 (Table 4). The second scenario represents the base case used earlier to evaluate the basic structure  
911 of the SBE results and perform a sensitivity analysis. The minimum and maximum bounds of ranges  
912 of input conditions were set to differ by a factor of 2-3 in that scenario. This resulted in a log-normal

913 distribution of estimated sediment budgets (Figs. 3d & 11b). An over-confident geologist may  
914 ascertain uncertainty bounds of +/-10 %, which is normally only possible under controlled laboratory  
915 conditions or in modern systems with high-fidelity monitoring. This over-confidence leads to  
916 sediment budget predictions that approaches a normal distribution, closely centered around the  $p_{50}$   
917 (Fig. 11a). A scenario with broad uncertainty (a factor 5 difference between minimum and maximum  
918 input conditions, Table 4) results in an increasing relative likelihood that the sediment budget is  
919 small, but very large values also considered a possibility (Fig. 11c). The mode and median of the  
920 predictions start to diverge strongly for this broad range in uncertainty. Finally, in the virtual absence  
921 of geological constraints (Table 4), the most likely predicted sediment budget approaches  $0 \text{ km}^3$ ,  
922 while the  $p_{10}$ ,  $p_{50}$ , and  $p_{90}$  explode to  $20 \text{ km}^3$ ,  $3 \cdot 10^4 \text{ km}^3$ , and  $1 \cdot 10^6 \text{ km}^3$  respectively, the latter being  
923 of comparable scale to the Bengal Fan sediment budget (Curry, 1994). The degree of geological  
924 uncertainty is directly linked to the shape of the Probability Density Function (PDF) of the system's  
925 sediment-budget estimations (Fig. 11). The shape of these PDFs transition into each other with  
926 growing levels of uncertainty. This implies that the distributions are in fact all realizations of a single  
927 family of PDFs such as the binomial Poisson functions, or gamma or lognormal distributions. All of  
928 these statistical families are two and one-parameter functions. The premise is then that it should be  
929 possible to parameterize the distribution of sediment budgets directly from the boundary conditions,  
930 without the need of the Monte Carlo realizations of the SBE. This mathematical exercise is not  
931 pursued herein.

932 The predictions of sediment budgets in the absence of a geological model were, perhaps  
933 unsurprisingly, that any amount of sediment might have gone through these channels, yet that the  
934 most likely amount converges to nothing. Process-based prediction of sediment budget is thus not  
935 possible in absence of geological constraints on the model. This insight justifies continued efforts by  
936 the sedimentological community to try to understand the expression of turbidity current processes in  
937 the stratigraphic record. It also underscores the need for modelers and stratigraphers to engage in

938 integrated projects. This should motivate the research community to strive for integrated studies  
939 with research teams involving both experts in stratigraphy and sediment transport processes.

940         **Complexity** --- While the SBE results are consistent with known cases at the largest and  
941 smallest scales, the simulated flow structures in fact differ for the different scales (Fig. 6 vs. 7 & 9).  
942 Specifically, the real world flows are more stratified at their base, meaning that the near-bed  
943 gradients in suspended sediment concentration are larger in nature than in small scale laboratory  
944 experiments. Another striking feature is that the SBE captures the similarity of scale in flow velocity  
945 between real world (Tres Pasos) and experimental flows (order 1 m/s), despite the 2 orders of  
946 magnitude difference in flow thickness. The fact that the SBE produces varying turbidity current  
947 structures at varying scales is a sign that while it is a simple model, it is still complex enough to yield  
948 results that cannot be foreseen and that fulfill the essential requirement of any model: we can learn  
949 something new about the process from the model results.

950 Empirical relations obtained by fitting small-scale experimental data cannot readily be extrapolated  
951 to full field scale, because there is always the concern of extrapolating beyond the parameter space  
952 for which the relation was originally obtained. Understanding of the physical processes, however, can  
953 be based on small scale experiments, because the equations that describe the physical process can  
954 yield different predictions at different scales. This is illustrated by the ability of the SBE to simulate  
955 strongly stratified, high- $r_o$  turbidity currents at field scale while many of the ideas were justified from  
956 scientific studies of small scale experiments with poorly stratified flows. It further demonstrates that  
957 the aim of an experimental study in sedimentology can, and should be to learn more about nature,  
958 not to learn more about the laboratory. We suggest that researchers modelling turbidity currents at  
959 the full natural scale consider highly stratified flows with  $r_o \sim 10$ , in future work, rather than the  
960 customary weakly stratified values of 1.6-2.0. Better still, since the input conditions of the SBE are a  
961 limited subset of the boundary conditions required for depth-averaged modelling of turbidity  
962 currents, such models could *a priori* query the SBE to obtain an estimate for  $r_o$ . These considerations  
963 are an illustration of how more simple models can be used to direct more complex models to more

964 relevant segments of their parameter space, and how model integration between simple and more  
965 complex models can improve the relevance of simulations performed.

966 More complex modelling workflows exist for turbidity-current research that addresses questions  
967 beyond bulk sediment budgets. It is tempting to select one of these more complex approaches in the  
968 pursuit of higher-fidelity results. However, a potential pitfall is that more intricate model systems are  
969 in practice associated with more parameters and variables and will therefore require the user to set  
970 more intricate and precise boundary conditions, i.e. to be more knowledgeable about the system *a*  
971 *priori*. This is a problem especially in ancient systems, where parameters such as bathymetry can  
972 have a controlling effect on modelled turbidity currents, yet are essentially unresolved at the  
973 resolution needed for high-fidelity simulations (Aas *et al.*, 2010). The model presented in this paper  
974 has purposefully been designed with many simplifications, so that it can serve as the first, quick,  
975 check of a system's range of parameters, either as the final stage in sediment budget estimation  
976 workflows, or ahead of more concerted modelling efforts with higher-fidelity modelling approaches.

977 The benefits of the simplified modeling approach of the SBE that have been emphasized in this  
978 discussion do not preclude meaningful future extensions of the model. One desirable extension could  
979 be to include physics-based modelling of the concentration profile, the shape of which is now  
980 included with a crude exponential equation; another is the incorporation of grain-size distributions  
981 within the concentration profiles. Another useful added complexity could be distinction between  
982 flow structure and sediment flux in short duration, dense, thin, fast, frontal cells and extended (in  
983 time), dilute, quasi-steady phases that have recently been described in monitoring studies (Azpiroz-  
984 Zabala *et al.*, 2017; Simmons *et al.*, 2020; Wang *et al.*, 2020). These different phases of events could  
985 have different roles in the sediment fluxes along deep-marine systems, while the initial version of the  
986 SBE presented here assumes a single, steady flow structure during the entire event duration. Such  
987 extensions of the SBE, however, should not come at the expense of the core virtues of the SBE as  
988 called for by Sømme and Martinsen (2017): a simple, quantitative model, which reflects natural  
989 variability and can be applied to ancient systems.

990

991

## CONCLUSIONS

992 We presented the Sediment Budget Estimator, a simplified, robust model that links the flow

993 structure of turbidity currents to observable submarine channel characteristics. The SBE uses this

994 structure for stochastic first order predictions of sediment fluxes and budgets in channelized

995 turbidity current systems. The model has been structured such that all necessary input conditions

996 can be obtained from geological or oceanographic observations or published analogue datasets.

997 A sensitivity analysis reveals that fundamental uncertainty about the sediment concentration of

998 turbidity currents has the largest impact on variability of sediment budget predictions. Channel width

999 also has a marked effect. Aspects of timing of turbidity currents (recurrence time, duration of

1000 individual flows, and duration of the geological activity of the system) all have linear influences on

1001 uncertainty. Channel depth is less influential and the slope of the system has a surprisingly modest

1002 effect on the results.

1003 The SBE is successfully validated against small scale laboratory experiments and the 1929 Grand

1004 Banks turbidity current, with sediment budgets that differ by 12 orders of magnitude.

1005 Application of the model to slope-channel deposits of the Cretaceous Tres Pasos Formation

1006 demonstrates the potential for paleo sediment-budget estimations. Intra channel-deposit surfaces

1007 with a vertical amplitude of 2.5-6.5 m are associated with formative turbidity currents. Alternative,

1008 less likely, associations between formative currents and channel element or channel complex scales

1009 yield budget estimates that are 1 or 2 orders of magnitude too large, respectively. The estimates of

1010 sediment budget for the lifespan of a single channel element offer an inroad into estimation of lobe

1011 element, lobe, and fan volumes. These can in turn be correlated to metrics of the slope, shelf, and

1012 catchment segments of the source-to-sink system. In such a comprehensive source to sink analysis

1013 the SBE can be applied in together with existing sediment budget estimators for catchment areas and

1014 fluvial systems, such as BQART and the Fulcrum approach for fluvial paleohydrology.



1015 Application of the SBE to submarine channels and their deposits in modern sea-floor settings,  
1016 geological outcrops of ancient systems, and subsurface datasets will enable first order flux and  
1017 budget predictions and reconstructions of sediment and other phases.

1018

1019

### **SUPPORTING MATERIAL**

1020 The Matlab scripts that constitute the Sediment Budget Estimator have been published on Github  
1021 (Eggenhuisen and Tilston, 2022): <https://github.com/JorisEggenhuisen/SBE> . Input conditions for the  
1022 simulations discussed in this paper are supplied in the same repository. .

1023

1024

### **ACKNOWLEDGMENTS**

1025 JTE, MT, FP, JdL, and YS acknowlegde funding of the EuroSEDS project by NWO (grant NWO-  
1026 864.13.006), ExxonMobil, Shell, and Equinor.

1027 Discussions with Michal Janocko helped direct the functionality of the SBE at an early stage.

1028 The participants of the Utrecht University MSc course Dynamics of Sedimentary Systems (2018-2021)  
1029 are gratefully acknowledged for testing the SBE. Their course work pointed out the bugs and benefits  
1030 of the SBE. Their collective success in using the SBE to constrain sediment budgets in diverse deep-  
1031 water systems has provided the necessary motivation to carry this manuscript to completion.

1032 Reviewers Zane Jobe and Oriol Falivene, and Associate Editor Jake Covault, provided constructive  
1033 comments that helped us improve our paper.

1034

1035

### **REFERENCES**

1036 Aas, T.E., Howell, J.A., Janocko, M., and Jackson, C.A.L., 2010, Control of Aptian palaeobathymetry on  
1037 turbidite distribution in the Buchan Graben, Outer Moray Firth, Central North Sea: Marine and  
1038 Petroleum Geology, v. 27, 412–434.

1039 Abd El-Gawad, S., Cantelli, A., Pirmez, C., Minisini, D., Sylvester, Z., and Imran, J., 2012, Three-

1040 dimensional numerical simulation of turbidity currents in a submarine channel on the seafloor

1041 of the Niger Delta slope: *Journal of Geophysical Research*, v. 117, C05026.

1042 Allen, J.R.L., 1991, The Bouma division A and the possible duration of turbidity currents: *Journal of*  
1043 *Sedimentary Petrology*, v. 61, p. 291–295.

1044 Allin, J.R., Hunt, J.E., Clare, M.A., and Talling, P.J., 2018, Eustatic sea-level controls on the flushing of a  
1045 shelf-incising submarine canyon: *GSA Bulletin*, v. 130, p. 222–237.

1046 Altinakar, M.S., Graf, W.H., and Hopfinger, E.J., 1996, Flow structure in turbidity currents: *Journal of*  
1047 *Hydraulic Research*, v. 34, p. 713–718.

1048 Amblas, D., Canals, M., Urgeles, R., Lastras, G., Liqueste, C., Hughes-Clarke, J.E., Casamor, J.L., and  
1049 Calafat, A.M., 2006, Morphogenetic mesoscale analysis of the northeastern Iberian margin, NW  
1050 Mediterranean Basin: *Marine Geology*, v. 234, p. 3–20.

1051 Anderson, J.B., Wallace, D.J., Simms, A.R., Rodriguez, A.B., Weight, R.W.R., and Taha, Z.P., 2016,  
1052 Recycling sediments between source and sink during a eustatic cycle: *Systems of late*  
1053 *Quaternary northwestern Gulf of Mexico Basin: Earth-Science Reviews*, v. 153, p. 111–138.

1054 Arfaie, A., Burns, A.D., Dorrell, R.M., Eggenhuisen, J.T., Ingham, D.B., and McCaffrey, W.D., 2014,  
1055 Optimised mixing and flow resistance during shear flow over a rib roughened boundary:  
1056 *International Communications in Heat and Mass Transfer*, v. 107, p. 141–147.

1057 Azpiroz-Zabala, M., Cartigny, M.J.B., Talling, P.J., Parsons, D.R., Sumner, E.J., Clare, M.A., Simmons,  
1058 S.M., Cooper, C., and Pope, E.L., 2017, Newly recognized turbidity current structure can explain  
1059 prolonged flushing of submarine canyons: *Science Advances*, v. 3, e1700200.

1060 Baas, J.H., van Dam, R.L., and Storms, J.E.A., 2000, Duration of deposition from decelerating high-  
1061 density turbidity currents: *Sedimentary Geology*, v. 136, p. 71–88.

1062

1063 Basani, R., Janocko, M., Cartigny, M.J.B., Hansen, W.M., and Eggenhuisen, J.T., 2014, MassFLOW-3D  
1064 as a simulation tool for turbidity currents: some preliminary results. IAS, Speical Publication 46,  
1065 p. 587–608.

1066 Beelen, D., Jackson, C.A.L., Patruno, S., Hodgson, D.M., and Alexandre, J.P.T., 2019, The effects of

1067 differential compaction on clinothem geometries and shelf-edge trajectories, *Geology*, v. 47, p.  
1068 1011–1014.

1069 Best, J.L., Kirkbride, A.D., and Peakall, J., 2001, Mean flow and turbulence structure of sediment-  
1070 laden gravity currents: new insights using ultrasonic Doppler velocity profiling: IAS, Special  
1071 Publication 31, p. 159–172.

1072 Bhattacharya, J.P., Copeland, P., Lawton, T.F., and Holbrook, J., 2016, Estimation of source area , river  
1073 paleo-discharge , paleoslope , and sediment budgets of linked deep-time depositional systems  
1074 and implications for hydrocarbon potential: *Earth-Science Reviews*, v. 153, p. 77–110.

1075 Bolla Pittaluga, M., Frascati, A., and Falivene, O., 2018, A gradually varied approach to model  
1076 turbidity currents in submarine channels: *Journal of Geophysical Research Earth Surface*, v. 123,  
1077 p. 80–96.

1078 Burgess, P.M., and Hovius, N., 1998, Rates of delta progradation during highstands: Consequences for  
1079 timing of deposition in deep-marine systems: *Journal of the Geological Society*, v. 155, p. 217–  
1080 222.

1081 Cantero, M.I., Balachandar, S., and Parker, G., 2009, Direct numerical simulation of stratification  
1082 effects in a sediment- laden turbulent channel flow: *Journal of Turbulence*, v. 10, p. 37–41.

1083 Cantero, M.I., Cantelli, A., Pirmez, C., Balachandar, S., Mohrig, D., Hickson, T.A., Yeh, T., Naruse, H.,  
1084 and Parker, G., 2011, Emplacement of massive turbidites linked to extinction of turbulence in  
1085 turbidity currents: *Nature Geoscience*, v. 5, p. 42–45.

1086 Cantero, M.I., Shringarpure, M., and Balachandar, S., 2012, Towards a universal criteria for  
1087 turbulence suppression in dilute turbidity currents with non-cohesive sediments: *Geophysical*  
1088 *Research Letters*, v. 39, L14603.

1089 Cartigny, M.J.B., Eggenhuisen, J.T., Hansen, E.W.M., and Postma, G., 2013, Concentration-dependent  
1090 flow stratification in experimental high-density turbidity currents and their relevance to  
1091 turbidite facies models: *Journal of Sedimentary Research*, v. 83, p. 1047–1065.

1092 Carvajal, C.R., and Steel, R.J., 2006, Thick turbidite successions from supply-dominated shelves during

- 1093 sea-level highstand: *Geology*, v. 34, p. 665–668.
- 1094 Champagne, F.H., Pao, Y.H., and Wygnanski, I.J., 1976, On the two-dimensional mixing region: *J. Fluid*  
1095 *Mech.*, v. 74, p. 209–250.
- 1096 Chang, H.H., 1988, Fluvial processes in river engineering: *Krieger*, Malabar, Florida, 446 p.
- 1097 Choux, C.M.A., Baas, J.H., McCaffrey, W.D., and Haughton, P.D.W., 2005, Comparison of spatio-  
1098 temporal evolution of experimental particulate gravity flows at two different initial  
1099 concentrations, based on velocity, grain size and density data: *Sedimentary Geology*, v. 179, p.  
1100 49–69.
- 1101 Clare, M.A., Hughes Clarke, J.E., Talling, P.J., Cartigny, M.J.B., and Pratomo, D.G., 2016,  
1102 Preconditioning and triggering of offshore slope failures and turbidity currents revealed by most  
1103 detailed monitoring yet at a fjord-head delta: *Earth and Planetary Science Letters*, v. 450, p.  
1104 208–220.
- 1105 Clare, M.A., Talling, P.J., Challenor, P., Malgesini, G., and Hunt, J., 2014, Distal turbidites reveal a  
1106 common distribution for large (>0.1 km<sup>3</sup>) submarine landslide recurrence: *Geology*, v. 42, p.  
1107 263–266.
- 1108 Clarke, J.E.H., 2016, First wide-angle view of channelized turbidity currents links migrating cyclic steps  
1109 to flow characteristics: *Nature Communications*, v. 7, 11896.
- 1110 Cooper, C., 2013, Turbidity Current Measurements in the Congo Canyon: Offshore Technololy  
1111 Conference, 23992.
- 1112 Covault, J.A., Fildani, A., Romans, B.W., and McHargue, T., 2011, The natural range of submarine  
1113 canyon-and-channel longitudinal profiles: *Geosphere*, v. 7, p. 313–332.
- 1114 Covault, J.A., Normark, W.R., Romans, B.W., and Graham, S.A., 2007, Highstand fans in the California  
1115 borderland: The overlooked deep-water depositional systems: *Geology*, v. 35, p. 783–786.
- 1116 Covault, J.A., Sylvester, Z., Ceyhan, C., and Dunlap, D.B., 2021, Giant meandering channel evolution,  
1117 Campos deep-water salt basin, Brazil: *Geosphere*, v. 17, p. 1869–1889.
- 1118 Crabaugh, J.P., and Steel, R.J., 2004, Basin-floor fans of the Central Tertiary Basin, Spitsbergen:

1119 relationship of basin-floor sand-bodies to prograding clinoforms in a structurally active basin:  
1120 Geological Society, London, Special Publications, v. 222, p. 187–208.

1121 Cullis, S., Colombera, L., Patacci, M., and McCaffrey, W.D., 2018, Hierarchical classifications of the  
1122 sedimentary architecture of deep-marine depositional systems: *Earth-Science Reviews*, v. 179,  
1123 p. 38–71.

1124 Curray, J.R., 1994, Sediment volume and mass beneath the Bay of Bengal. *Earth and Planetary  
1125 Science Letters*, v. 125, p. 371–383.

1126 Daly, R.A., 1936, Origin of Submarine “Canyons”: *American Journal of Science*, v. 31, p. 401–420.

1127 Daniels, B.G., Auchter, N.C., Hubbard, S.M., Romans, B.W., Matthews, W.A., and Stright, L., 2018,  
1128 Timing of deep-water slope evolution constrained by large-n detrital and volcanic ash zircon  
1129 geochronology, Cretaceous Magallanes Basin, Chile: *GSA Bulletin*, v. 130, p. 438–454.

1130 Dorrell, R.M., Darby, S.E., Peakall, J., Sumner, E.J., Parsons, D.R., and Wynn, R.B., 2014, The critical  
1131 role of stratification in submarine channels: Implications for channelization and long runout of  
1132 flows: *Journal of Geophysical Research Oceans*, v. 119, p. 2620–2641.

1133 Eggenhuisen, J.T., Cartigny, M.J.B., and de Leeuw, J., 2017, Physical theory for near-bed turbulent  
1134 particle suspension capacity: *Earth Surface Dynamics*, v. 5, p. 269–281.

1135 Eggenhuisen, J.T. and McCaffrey, W.D., 2012, The vertical turbulence structure of experimental  
1136 turbidity currents encountering basal obstructions: implications for vertical suspended  
1137 sediment distribution in non-equilibrium currents: *Sedimentology*, v. 59, p. 1101–1120.

1138 Eggenhuisen, J.T., and Tilston, M.C., 2022, Sediment Budget Estimator for deep marine depositional  
1139 systems (1.0.0). Zenodo. <https://doi.org/10.5281/zenodo.6635519>.

1140 Eggenhuisen, J.T., Tilston, M.C., Leeuw, J., Pohl, F., and Cartigny, M.J.B., 2019, Turbulent diffusion  
1141 modelling of sediment in turbidity currents: An experimental validation of the Rouse approach:  
1142 *The Depositional Record*, v. 6, p. 203–216.

1143 Ellison, T.H., and Turner, J.S., 1959, Turbulent entrainment in stratified flows: *Journal of Fluid*

1144 Mechanics, v. 6, p. 423–448.

1145 Falivene, O., Prather, B.E. and Martin, J., 2020, Quantifying sand delivery to deep water during  
1146 changing sea-level: Numerical models from the Quaternary Brazos Icehouse continental margin.  
1147 Basin Research, v. 32, p. 1711–1733.

1148 Garcia, M. and Parker, G., 1993, Experiments on the entrainment of sediment into suspension by a  
1149 dense bottom current: Journal of Geophysical Research, v. 98, p. 4793–4807.

1150 Garcia, M. and Parker, G., 1989, Experiments on hydraulic jumps in turbidity currents near a canyon-  
1151 fan transition: Science, v. 245, p. 393–396.

1152 Garcia, M.H., 1994, Depositional turbidity currents laden with poorly sorted sediment: Journal of  
1153 Hydraulic Engineering, v. 120, p. 1240–1263.

1154 García, M.H., 2008, Sedimentation engineering: *American Society of Civil Engineers*, Reston, Virginia,  
1155 USA, 1132 p.

1156 Gray, T.E., Alexander, J. and Leeder, M.R., 2005, Quantifying velocity and turbulence structure in  
1157 depositing sustained turbidity currents across breaks in slope: *Sedimentology*, 52, 467–488.

1158 Grundvag, S.-A., Johannessen, E.P., Helland-hansen, W., and Plink-Bjorklund, P., 2014, Depositional  
1159 architecture and evolution of progradationally stacked lobe complexes in the Eocene Central  
1160 Basin of Spitsbergen: *Sedimentology*, v. 61, p. 535–569.

1161 Halsey, T.C., Kumar, A., and Perillo, M.M., 2017, Sedimentological regimes for turbidity currents:  
1162 Depth-averaged theory: *Journal of Geophysical Research Oceans*, v. 122, C012635.

1163 Hamilton, P., Gaillot, G., Strom, K., Fedele, J., and Hoyal, D., 2017, Linking hydraulic properties in  
1164 supercritical submarine distributary channels to depositional-lobe geometry: *Journal of*  
1165 *Sedimentary Research*, v. 87, p. 935–950.

1166 Heerema, C.J., Talling, P.J., Cartigny, M.J., Paull, C.K., Bailey, L., Simmons, S.M., Parsons, D.R., Clare,  
1167 M.A., Gwiazda, R., Lundsten, E., Anderson, K., Maier, K.L., Xu, J.P., Sumner, E.J., Rosenberger, K.,  
1168 Gales, J., McGann, M., Carter, L., and Pope, E., 2020, What determines the downstream  
1169 evolution of turbidity currents?: *Earth and Planetary Science Letters*, v. 532, 116023.

1170 Heezen, B.C., and Ewing, M., 1952, Turbidity currents and submarine slumps, and the 1929 Grand  
1171 Banks earthquake: *American Journal of Science*, v. 250, p. 849–873.

1172 Heijnen, M.S., Clare, M.A., Cartigny, M.J.B., Talling, P.J., Hage, S., Pope, E.L., Bailey, L., Sumner, E.,  
1173 Gwyn Lintern, D., Stacey, C., Parsons, D.R., Simmons, S.M., Chen, Y., Hubbard, S.M.,  
1174 Eggenhuisen, J.T., Kane, I., and Hughes Clarke, J.E., 2022, Fill, flush or shuffle: How is sediment  
1175 carried through submarine channels to build lobes? *Earth and Planetary Science Letters*, v. 584,  
1176 117481.

1177 Helland-Hansen, W., Sømme, T.O.R.O., Martinsen, O.L.E.J., Lunt, I.A.N., and Thurmond, J., 2016,  
1178 Deciphering Earth’s natural hourglasses: perspectives on source-to-sink analysis: *Journal of*  
1179 *Sedimentary Research*, v. 86, p. 1008–1033.

1180 Hermidas, N., Eggenhuisen, J.T., Jacinto, R.S., Luthi, S.M., Toth, F., and Pohl, F., 2018, A Classification  
1181 of Clay-Rich Subaqueous Density Flow Structures: *Journal of Geophysical Research Earth*  
1182 *Surface*, v. 123, p. 945–966.

1183 Hiscott, R.N., Hall, F.R., and Pirmez, C., 1997, Turbidity-current overspill from the Amazon Channel :  
1184 Texture of the silt/sand load, paleoflow from anisotropy of magnetic susceptibility and  
1185 implications for flow processes: *Proceedings of the Ocean Drilling Program, Scientific results*, v.  
1186 155, p. 53–78.

1187 Hizzett, J.L., Hughes Clarke, J.E., Sumner, E.J., Cartigny, M.J.B., Talling, P.J., and Clare, M.A., 2018,  
1188 Which Triggers Produce the Most Erosive, Frequent, and Longest Runout Turbidity Currents on  
1189 Deltas?: *Geophysical Research Letters*, v. 45, p. 855–863.

1190 Holbrook, J., and Wanas, H., 2014, A fulcrum approach to assessing source-to-sink mass balance  
1191 using channel paleohydrologic paramaters derivable from common fluvial data sets with an  
1192 example from the cretaceous of Egypt: *Journal of Sedimentary Research*, v. 84, p. 349–372.

1193 Hubbard, S.M., Covault, J.A., Fildani, A., and Romans, B.W., 2014, Sediment transfer and deposition in  
1194 slope channels: Deciphering the record of enigmatic deep-sea processes from outcrop: *GSA*  
1195 *Bulletin*, v. 126, p. 857–871.

1196 Hubbard, S.M., Fildani, A., Romans, B.W., Covault, J.A., and McHargue, T.R., 2010, High-Relief Slope  
1197 Cliniform Development: Insights from Outcrop, Magallanes Basin, Chile: *Journal of Sedimentary*  
1198 *Research*, v. 80, p. 357–375.

1199 Hubbard, S.M., Jobe, Z.R., Romans, B.W., Covault, J.A., Sylvester, Z., and Fildani, A., 2020, The  
1200 stratigraphic evolution of a submarine channel: Linking seafloor dynamics to depositional  
1201 products: *Journal of Sedimentary Research*, v. 90, p. 673–686.

1202 Hughes Clarke, J.E., 2016, First wide-angle view of channelized turbidity currents links migrating cyclic  
1203 steps to flow characteristics: *Nature Communications*, v. 7, p. 11896.

1204 Hughes Clark, J.E., Shor, A.N., Piper, D.J.W., and Mayer, L.A., 1990, Large-scale current-induced  
1205 erosion and deposition in the path of the 1929 Grand Banks turbidity current: *Sedimentology*, v.  
1206 37, p. 613–629.

1207 Islam, M.A. and Imran, J., 2010, Vertical structure of continuous release saline and turbidity currents:  
1208 *Journal of Geophysical Research*, v. 115, C08025.

1209 Jobe, Z.R., Lowe, D.R., and Morris, W.R., 2012, Climbing-ripple successions in turbidite systems:  
1210 Depositional environments, sedimentation rates and accumulation times: *Sedimentology*, v. 59,  
1211 p. 867–898.

1212 Jobe, Z.R., Sylvester, Z., Parker, A.O., Howes, N., Slowey, N., and Pirmez, C., 2015, Rapid Adjustment  
1213 of Submarine Channel Architecture To Changes in Sediment Supply: *Journal of Sedimentary*  
1214 *Research*, v. 85, p. 729–753.

1215 Jobe, Z., Sylvester, Z., Bolla Pittaluga, M., Frascati, A., Pirmez, C., Minisini, D., Howes, N., and Cantelli,  
1216 A., 2017, Facies architecture of submarine channel deposits on the western Niger Delta slope:  
1217 Implications for grain-size and density stratification in turbidity currents: *Journal of Geophysical*  
1218 *Research Earth Surface*, v. 122, p. 473–491.

1219 Jobe, Z.R., Howes, N., Romans, B.W., and Covault, J.A., 2018, Volume and recurrence of submarine-  
1220 fan-building turbidity currents: *The Depositional Record*, v. 4, p. 160–176.

1221 Johannessen, E.P. and Steel, R.J., 2005, Shelf-margin clinofolds and prediction of deepwater sands:



1222 Basin Research, v. 17, p. 521–550.

1223 Kane, I.A., Ponten, A.S.M., Vangdal, B., Eggenhuisen, J.T., Hodgson, D.M., and Spychala, Y.T., 2017,  
1224 The stratigraphic record and processes of turbidity current transformation across deep-marine  
1225 lobes: Sedimentology, v. 64, p. 1236–1273.

1226 Khripounoff, A., Vangriesheim, A., Babonneau, N., Crassous, P., Dennielou, B., and Savoye, B., 2003,  
1227 Direct observation of intense turbidity current activity in the Zaire submarine valley at 4000 m  
1228 water depth: Marine Geology, v. 194, p. 151–158.

1229 Kneller, B., 2003, The influence of flow parameters on turbidite slope channel architecture: Marine  
1230 and Petroleum Geology, v. 20, p. 901–910.

1231 Kneller, B. and Buckee, C., 2000, The structure and fluid mechanics of turbidity currents: a review of  
1232 some recent studies and their geological implications: Sedimentology, v. 47, p. 62–94.

1233 Kneller, B., Nasr-Azadani, M.M., Radhakrishnan, S., and Meiburg, E., 2016, Long-range sediment  
1234 transport in the world's oceans by stably stratified turbidity currents: Journal of Geophysical  
1235 Research Oceans, v. 121, p. 8608–8620.

1236 Kneller, B.C., Bennett, S.J., and McCaffrey, W.D., 1999, Velocity structure, turbulence and fluid  
1237 stresses in experimental gravity currents: Journal of Geophysical Research, v. 104, 5381-5391.

1238 Konsoer, K., Zinger, J., and Parker, G., 2013, Bankfull hydraulic geometry of submarine channels  
1239 created by turbidity currents: Relations between bankfull channel characteristics and formative  
1240 flow discharge: Journal of Geophysical Research Earth Surface, v. 118, p. 216–228.

1241 Krastel, S., Braeunig, A., Feldens, P., Georgiopoulou, A., Jaehmlich, H., Lange, M., Lindhorst, K.,  
1242 Llopart, J., Mader, S., Mehringer, L., Merl, M., Muecke, I., Renkl, C., Roskoden, R., M, S.,  
1243 Schulten, I., Scharwz, J.-P., Stevenson, C., Vallee, M., Wegener, B., and Wiesenber, L., 2016,  
1244 Geomorphology, processes and geohazards of giant submarine landslides and tsunami  
1245 generation capacity, as recorded in the sedimentary record of the only historic slide of this kind:  
1246 the 1929 Grand Banks landslide of the Canadian Atlantic continental margin: *MARIA S. MERIAN-*  
1247 *Berichte*, MSM47, 55 p.

- 1248 Kuenen, P.H., 1952, Estimated size of the Grand Banks turbidity current: *American Journal of Science*,  
1249 v. 250, p. 874–884.
- 1250 Lastras, G., Canals, M., Amblas, D., Lavoie, C., Church, I., De Mol, B., Duran, R., Calafat, A.M., Hughes-  
1251 Clarke, J.E., Smith, C.J., and Heussner, S., 2011, Understanding sediment dynamics of two large  
1252 submarine valleys from seafloor data: Blanes and La Fonera canyons, northwestern  
1253 Mediterranean Sea: *Marine Geology*, v. 280, p. 20–39.
- 1254 Lee, S.E., Talling, P.J., Ernst, G.G.J., and Hogg, A.J., 2002, Occurrence and origin of submarine plunge  
1255 pools at the base of the US continental slope: *Marine Geology*, v. 185, p. 363–377.
- 1256 de Leeuw, J., Eggenhuisen, J.T., and Cartigny, M.J.B., 2016, Morphodynamics of submarine channel  
1257 inception revealed by new experimental approach: *Nature Communications*, v. 7, 10886.
- 1258 de Leeuw, J., 2017, The sedimentary record of submarine channel morphodynamics, [PhD thesis]:  
1259 Utrecht University, Utrecht, 149 p.
- 1260 de Leeuw, J., Eggenhuisen, J.T., and Cartigny, M.J.B., 2018a, Linking submarine channel–levee facies  
1261 and architecture to flow structure of turbidity currents: insights from flume tank experiments:  
1262 *Sedimentology*, v. 65, p. 931–951.
- 1263 de Leeuw, J., Eggenhuisen, J.T., Spychala, Y.T., Heijnen, M.S., Pohl, F., and Cartigny, M.J.B., 2018b,  
1264 Sediment volume and grain-size partitioning between submarine channel–levee systems and  
1265 lobes: an experimental study: *Journal of Sedimentary Research*, v. 88, p. 777–794.
- 1266 Leopold, L.B., and Maddock, T.J., 1953, The hydraulic geometry of stream channels and some  
1267 physiographic implications: U.S. Geological Survey, professional paper 252, 57 p.
- 1268 Lin, W.E.N. and Bhattacharya, J.P., 2017, Estimation of source-to-sink mass balance by a fulcrum  
1269 approach using channel paleohydrologic parameters of the Cretaceous Dunvegan Formation,  
1270 Canada: *Journal of Sedimentary Research*, v. 87, p. 97–116.
- 1271 Lowe, D.R., 1982, Sediment gravity flows: II. Depositional models with special reference to the  
1272 deposits of high-density turbidity currents: *Journal of Sedimentary Research*, v. 52, p. 279–297.

1273 Macauley, R. V. and Hubbard, S.M., 2013, Slope channel sedimentary processes and stratigraphic  
1274 stacking, Cretaceous Tres Pasos Formation slope system, Chilean Patagonia: *Marine and*  
1275 *Petroleum Geology*, v. 41, p. 146–162.

1276 McHargue, T., Pyrcz, M.J., Sullivan, M.D., Clark, J.D., Fildani, A., Romans, B.W., Covault, J.A., Levy, M.,  
1277 Posamentier, H.W., and Drinkwater, N.J., 2011, Architecture of turbidite channel systems on the  
1278 continental slope: Patterns and predictions: *Marine and Petroleum Geology*, v. 28, p. 728–743.

1279 Middleton, G. V, 1966, Small-scale models of turbidity currents and the criterion for auto-suspension:  
1280 *Journal of Sedimentary Petrology*, v. 36, p. 202–208.

1281 Middleton, G. V, 1993, Sediment deposition from turbidity currents: *Annual Reviews in Earth and*  
1282 *Planetary Science*, v. 21, p. 89–114.

1283 Mohrig, D. and Buttle, J., 2007, Deep turbidity currents in shallow channels, *Geology*, v. 35, p. 155.

1284 Mulder, T., Savoye, B., Piper, D.J.W., and Syvitski, J.P.M., 1998: The Var submarine sedimentary  
1285 system: understanding Holocene sediment delivery processes and their importance to the  
1286 geological record: Geological Society of London, Special Publication 129, p. 145–166.

1287 Paola, C. and Martin, J.M., 2012, Mass-balance effects in depositional systems: *Journal of*  
1288 *Sedimentary Research*, v. 82, p. 435–450.

1289 Parker, G., 1982, Conditions for the ignition of catastrophically erosive turbidity currents: *Marine*  
1290 *Geology*, v. 46, p. 307–327.

1291 Parker, G., Fukushima, Y., and Pantin, H.M., 1986, Self-accelerating turbidity currents: *Journal of Fluid*  
1292 *Mechanics*, v. 171, p. 145–181.

1293 Parker, G., Garcia, M., Fukushima, Y., and Yu, W., 1987, Experiments on turbidity currents over an  
1294 erodible bed: *Journal of Hydraulic Research*, v. 25, p. 123–147.

1295 Patruno, S., Hampson, G.J., and Jackson, C.A.L., 2015, Quantitative characterisation of deltaic and  
1296 subaqueous clinoforms: *Earth-Science Reviews*, v. 142, p. 79–119.

1297 Patruno, S. and Helland-Hansen, W., 2018, Clinoform systems: Review and dynamic classification  
1298 scheme for shorelines, subaqueous deltas, shelf edges and continental margins: *Earth-Science*

- 1299           Reviews, v. 185, p. 202–233.
- 1300   Paull, C.K., Talling, P.J., Maier, K.L., Parsons, D., Xu, J., Caress, D.W., Gwiazda, R., Lundsten, E.M.,  
1301           Anderson, K., Barry, J.P., Chaffey, M., O’Reilly, T., Rosenberger, K.J., Gales, J.A., et al., 2018,  
1302           Powerful turbidity currents driven by dense basal layers: *Nature Communications*, v. 9, p. 4114.
- 1303   Pemberton, E.A.L., Hubbard, S.M., Fildani, A., Romans, B., and Stright, L., 2016, The stratigraphic  
1304           expression of decreasing confinement along a deep-water sediment routing system: Outcrop  
1305           example from southern Chile: *Geosphere*, v. 12, p. 114–134.
- 1306   Piper, D.J.W. and Aksu, A.E., 1987, The source and origin of the 1929 Grand Banks turbidity current  
1307           inferred from sediment budgets: *Geo-Marine Letters*, v. 7, p. 177–182.
- 1308   Piper, D.J.W. and Deptuck, M., 1997, Fine-grained turbidites of the Amazon Fan: facies  
1309           characterization and interpretation: *Proceedings of the Ocean Drilling Program, Scientific*  
1310           Results 155, p. 79–108.
- 1311   Piper, D.J.W., Shor, A.N., and Hughes Clark, J.E., 1988, The 1929 Grand Banks earthquake, slump, and  
1312           turbidity current: *GSA, Special Paper 229*, p. 77–92.
- 1313   Pirmez, C. and Imran, J., 2003, Reconstruction of turbidity currents in Amazon Channel: *Marine and*  
1314           *Petroleum Geology*, v. 20, p. 823–849.
- 1315   Pirmez, C., Prather, B.E., Mallarino, G., O’Hayer, W.W., Droxler, A.W., and Winker, C.D., 2012,  
1316           Chronostratigraphy of the Brazos–Trinity Depositional System, Western Gulf of Mexico:  
1317           Implications for Deepwater Depositional Models: *SEPM, Special Publication 99*, p. 111–143.
- 1318   Pittaluga, M.B. and Imran, J., 2014, *Journal of Geophysical Research : Earth Surface* A simple model  
1319           for vertical profiles of velocity and suspended sediment concentration in straight and curved  
1320           submarine channels: *Journal of Geophysical Research Earth Surface*, v. 119, p. 483–503.
- 1321   Plapp, J.E. and Mitchell, J.P., 1960, A hydrodynamic theory of turbidity currents: *Journal of*  
1322           *Geophysical Research*, v. 65, p. 983–992.
- 1323   Pohl, F., Eggenhuisen, J.T., Cartigny, M.J.B., Tilston, M., and Leeuw, J., 2020, The influence of a slope  
1324           break on turbidite deposits: an experimental investigation: *Marine Geology*, v. 424, 106160.

- 1325 Pope, E.L., Talling, P.J., Carter, L., Clare, M.A., and Hunt, J.E., 2017, Damaging sediment density flows  
1326 triggered by tropical cyclones: *Earth and Planetary Science Letters*, v. 458, p. 161–169.
- 1327 Pope, S.B., 2000, *Turbulent Flows: Cambridge University Press*, 771 pp.
- 1328 Posamentier, H.W., and Vail, P.R., 1988, Eustatic controls on clastic deposition II—Sequence and  
1329 systems tract models: *SEPM Special Publication 42*, p. 125–154.
- 1330 Prather, B.E., O’Byrne, C., Pirmez, C., and Sylvester, Z., 2016, Sediment partitioning, continental  
1331 slopes and base-of-slope systems: *Basin Research*, v. 29, p. 394-416.
- 1332 Prélat, A., Hodgson, D.M., and Flint, S.S., 2009, Evolution, architecture and hierarchy of distributary  
1333 deep-water deposits: a high-resolution outcrop investigation from the Permian Karoo Basin,  
1334 South Africa: *Sedimentology*, v. 56, p. 2132–2154.
- 1335 Prélat, A., Covault, J.A., Hodgson, D.M., Fildani, A., and Flint, S.S., 2010, Intrinsic controls on the range  
1336 of volumes, morphologies, and dimensions of submarine lobes: *Sedimentary Geology*, v. 232, p.  
1337 66–76.
- 1338 Reading, H.G. and Richards, M., 1994, Turbidite systems in deep-water basin margins classified by  
1339 grain size and feeder system: *AAPG Bulletin*, v. 78, p. 792–822.
- 1340 Reimchen, A.P., Hubbard, S.M., Stright, L., and Romans, B.W., 2016, Using sea-floor morphometrics  
1341 to constrain stratigraphic models of sinuous submarine channel systems: *Marine and Petroleum*  
1342 *Geology*, v. 77, p. 92–115.
- 1343 Richards, M., Bowman, M., and Reading, H., 1998, Submarine-fan systems I: characterization and  
1344 stratigraphic prediction: *Marine and Petroleum Geology*, v. 15, p. 689–717.
- 1345 van Rijn, L.C., 2011, *Principles of fluid flow and surface waves in rivers, estuaries, seas, and oceans:*  
1346 2011 edn. *Aqua Publications*.
- 1347 Romans, B.W., Castelltort, S., Covault, J.A., Fildani, A., and Walsh, J.P., 2016, Environmental signal  
1348 propagation in sedimentary systems across timescales: *Earth-Science Reviews*, v. 153, p. 7–29.
- 1349 Romans, B.W., Fildani, A., Hubbard, S.M., Covault, J.A., Fosdick, J.C., and Graham, S.A., 2011,  
1350 Evolution of deep-water stratigraphic architecture, Magallanes Basin, Chile: *Marine and*

1351 Petroleum Geology, v. 28, p. 612–628.

1352 Rouse, H., 1937, Modern Conceptions of the Mechanics of Fluid Turbulence: Transactions of the  
1353 American Society of Civil Engineers, v. 102, p. 463–543.

1354 Salles, T., Lopez, S., Eschard, R., Mulder, T., Euzen, T., and Cacas, M.-C., 2009, A turbidity-current  
1355 model to simulate impact of basin-scale forcing parameters: SEPM, Special Publication 92, p.  
1356 363–383.

1357 Samuel, A., Kneller, B., Raslan, S., Sharp, A., and Parsons, C., 2003, Prolific deep-marine slope  
1358 channels of the Nile Delta, Egypt: AAPG Bulletin, v. 87, p. 541–560.

1359 Sequeiros, O.E., 2012, Estimating turbidity current conditions from channel morphology: A Froude  
1360 number approach, Journal of Geophysical Research, v. 117, C04003.

1361 Sequeiros, O.E., Mosquera, R., and Pedocchi, F., 2018, Internal Structure of a Self-Accelerating  
1362 Turbidity Current: Journal of Geophysical Research Oceans, v. 123, p. 6260–6276.

1363 Sequeiros, O.E., Spinewine, B., Beaubouef, R.T., Sun, T., García, M.H., and Parker, G., 2010,  
1364 Characteristics of velocity and excess density profiles of saline underflows and turbidity currents  
1365 flowing over a mobile bed: Journal of Hydraulic Engineering, v. 136, p. 412–433.

1366 Sharma, S., Bhattacharya, J.P., and Richards, B., 2017, Source-to-sink sediment budget analysis of the  
1367 Cretaceous Ferron sandstone, Utah , U.S.A., using the fulcrum approach: Journal of Sedimentary  
1368 Research, v. 87, p. 594–608.

1369 Shumaker, L.E., Jobe, Z.R., and Graham, S.A., 2017, Evolution of submarine gullies on a prograding  
1370 slope: Insights from 3D seismic reflection data: Marine Geology, v. 393, p. 35–46.

1371 Shumaker, L.E., Jobe, Z.R., Johnstone, S.A., Pettinga, L.A., Cai, D., and Moody, J.D., 2018, Controls on  
1372 submarine channel-modifying processes identified through morphometric scaling relationships:  
1373 Geosphere, v. 14, p. 2171–2187.

1374 Simmons, S.M., Azpiroz-Zabala, M., Cartigny, M.J.B., Clare, M.A., Cooper, C., Parsons, D.R., Pope, E.L.,  
1375 Sumner, E.J., and Talling, P.J., 2020, Novel acoustic method provides first detailed  
1376 measurements of sediment concentration structure within submarine turbidity currents:

1377 Journal of Geophysical Research Oceans, v. 125, e2019JC015904.

1378 Sømme, T.O., Helland-hansen, W., Martinsen, O.J., and Thurmond, J.B., 2009a, Relationships  
1379 between morphological and sedimentological parameters in source-to-sink systems: A basis for  
1380 predicting semi-quantitative characteristics in subsurface systems: Basin Research, v. 21, p.  
1381 361–387.

1382 Sømme, T.O., Martinsen, O.J., and Thurmond, J.B., 2009b, Reconstructing morphological and  
1383 depositional characteristics in subsurface sedimentary systems: An example from the  
1384 Maastrichtian-Danian Ormen Lange system: Møre Basin, Norwegian Sea. AAPG Bulletin, v. 93, p.  
1385 1347–1377.

1386 Sømme, T.O., Piper, D.J.W., Deptuck, M.E., and Helland-Hansen, W., 2011, Linking Onshore-Offshore  
1387 Sediment Dispersal in the Golo Source-to-Sink System (Corsica, France) During the Late  
1388 Quaternary: Journal of Sedimentary Research, v. 81, p. 118–137.

1389 Sømme, T.O., and Martinsen, O.J., 2017, *Deep-water depositional systems conference*: The Geological  
1390 Society, London, 25-27th January 2017.

1391 Stacey, C.D., Hill, P.R., Talling, P.J., Enkin, R.J., Hughes Clarke, J., and Lintern, D.G., 2019, How  
1392 turbidity current frequency and character varies down a fjord-delta system: Combining direct  
1393 monitoring, deposits and seismic data: Sedimentology, v. 66, p. 1–31.

1394 Stacey, M.W. and Bowen, A.J., 1988, The vertical structure of density and turbidity currents: Theory  
1395 and observations: Journal of Geophysical Research, v. 93, p. 3528–3542.

1396 Stevens, T., Paull, C.K., Ussler, W., McGann, M., Buylaert, J.P., and Lundsten, E., 2014, The timing of  
1397 sediment transport down Monterey Submarine Canyon, offshore California: GSA Buletin, v. 126,  
1398 p. 103–121.

1399 Stevenson, C.J., Feldens, P., Georgiopoulou, A., Schönke, M., Krastel, S., Piper, D.J.W., Lindhorst, K.,  
1400 and Mosher, D., 2018, Reconstructing the sediment concentration of a giant submarine gravity  
1401 flow: Nature Communications, v. 9, p. 1–7.

1402 Stevenson, C.J., Jackson, C.A.-L., Hodgson, D.M., Hubbard, S.M., and Eggenhuisen, J.T., 2015, Deep-

1403 water sediment bypass: *Journal of Sedimentary Research*, v. 85, p. 1058-1081.

1404 Straub, K.M. and Mohrig, D., 2008, Quantifying the morphology and growth of levees in aggrading  
1405 submarine channels: *Journal of Geophysical Research Earth Surface*, v. 113, p. 1–20.

1406 Straub, K.M., Mohrig, D., McElroy, B., Buttles, J., and Pirmez, C., 2008, Interactions between turbidity  
1407 currents and topography in aggrading sinuous submarine channels: A laboratory study: *GSA*  
1408 *Bulletin*, v. 120, p. 368–385.

1409 Strong, N. and Paola, C., 2008, Valleys that never were: Time surfaces versus stratigraphic surfaces:  
1410 *Journal of Sedimentary Research*, v. 78, p. 579–593.

1411 Sylvester, Z., Deptuck, M.E., Prather, B.E., Pirmez, C., and Byrne, C.O., 2012, Seismic stratigraphy of a  
1412 shelf-edge delta and linked submarine channels in the northeastern Gulf of Mexico.: *SEPM*  
1413 *special publication*, v. 99, p. 31–59.

1414 Syvitsky, J.P.M. and Milliman, J.D., 2007, *Geology , geography , and humans battle for dominance*  
1415 *over the delivery of fluvial sediment to the coastal ocean: Journal of Geology*, v. 115, p. 1–19.

1416 Talling, P.J., Masson, D.G., Sumner, E.J., and Malgesini, G., 2012, Subaqueous sediment density flows:  
1417 *Depositional processes and deposit types: Sedimentology*, v. 59, p. 1937–2003.

1418 Talling, P.J., Paull, C.K., and Piper, D.J.W., 2013, How are subaqueous sediment density flows  
1419 triggered, what is their internal structure and how does it evolve? Direct observations from  
1420 monitoring of active flows: *Earth-Science Reviews*, v. 125, p. 244–287.

1421 Tilston, M., Arnott, R.W.C., Rennie, C.D., and Long, B., 2015, The influence of grain size on the  
1422 velocity and sediment concentration profiles and depositional record of turbidity currents:  
1423 *Geology*, v. 43, p. 839–842.

1424 Traer, M.M., Hilley, G.E., Fildani, A., and McHargue, T., 2012, The sensitivity of turbidity currents to  
1425 mass and momentum exchanges between these underflows and their surroundings: *Journal of*  
1426 *Geophysical Research Earth Surface*, v. 117, F01009.

1427 Walsh, J.P., Wiberg, P.L., Aalto, R., and Kuehl, S.A., 2016, Source-to-sink research: economy of the  
1428 Earth’s surface and its strata: *Earth-Science Reviews*, v. 153, p. 1–6.

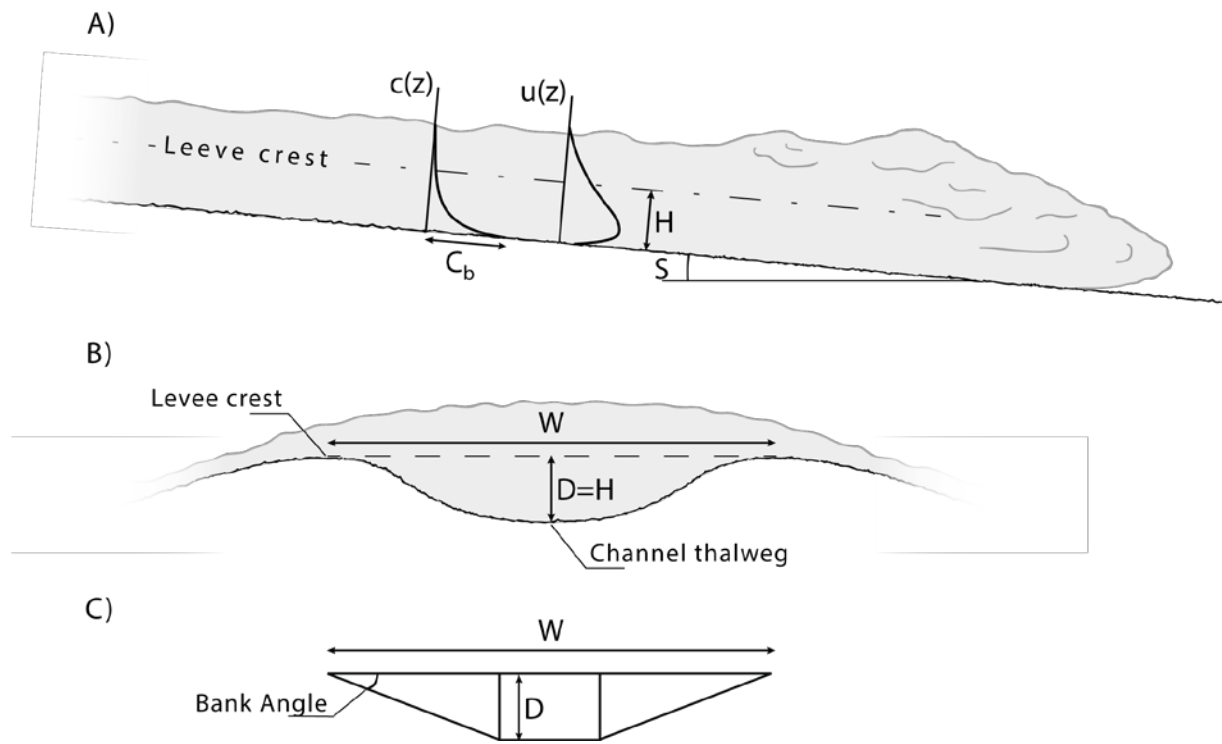


- 1429 Wang, Z., Xu, J., Talling, P.J., Cartigny, M.J.B., Simmons, S.M., Gwiazda, R., Paull, C.K., Maier, K.L., and  
1430 Parsons, D.R., 2020, Direct evidence of a high-concentration basal layer in a submarine turbidity  
1431 current: *Deep-Sea Research Part I: Oceanographic research Papers*, v. 161, 103300.
- 1432 Xu, J.P., Noble, M., Eittreim, S.L., Rosenfeld, L.K., Schwing, F.B., and Pilskaln, C.H., 2002, Distribution  
1433 and transport of suspended particulate matter in Monterey Canyon: *California, Marine Geology*,  
1434 v. 181, p. 215–234.
- 1435 Xu, J.P., 2011, Measuring currents in submarine canyons: Technological and scientific progress in the  
1436 past 30 years: *Geosphere*, v. 7, p. 868–876.
- 1437 Xu, J.P., Noble, M.A., and Rosenfeld, L.K., 2004, In-situ measurements of velocity structure within  
1438 turbidity currents: *Geophysical Research Letters*, v. 31, GL019718.
- 1439 Zeng, J., Lowe, D.R., Prior, D.B., Wiseman, W.J., and Bornhold, B.D., 1991, Flow properties of turbidity  
1440 currents in Bute Ilte, British Columbia: *Sedimentology*, v. 38, p. 975–996.
- 1441 Zhang, J., Burgess, P.M., Granjeon, D., and Steel, R., 2019, Can sediment supply variations create  
1442 sequences? Insights from stratigraphic forward modelling: *Basin Research*, v. 31, p. 274–289.

1443

1444

#### FIGURE CAPTIONS



1445

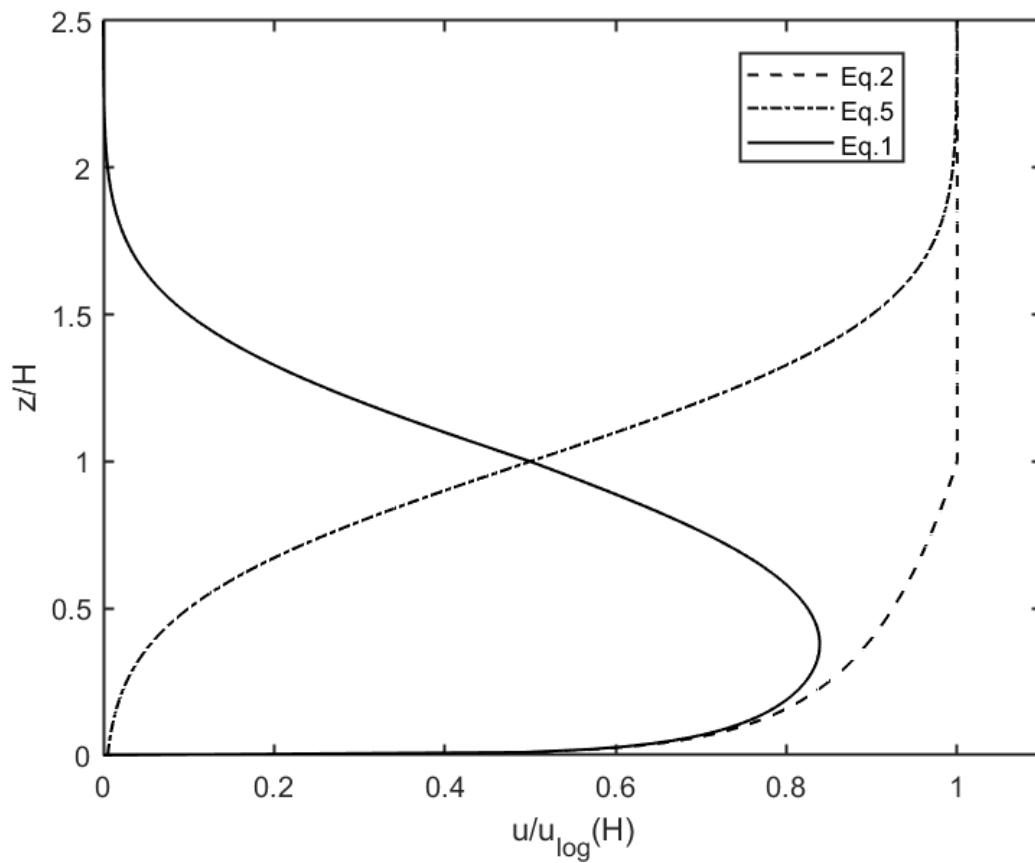
1446 **Fig. 1:** A) Schematic representation of the structure of a turbidity current, simplified from Altinakar et

1447 al. (1996). B) Schematic of the relation between channel cross-section and the modelled turbidity

1448 current. C) Trapezoidal cross-section of the model channel. The width of the rectangular thalweg

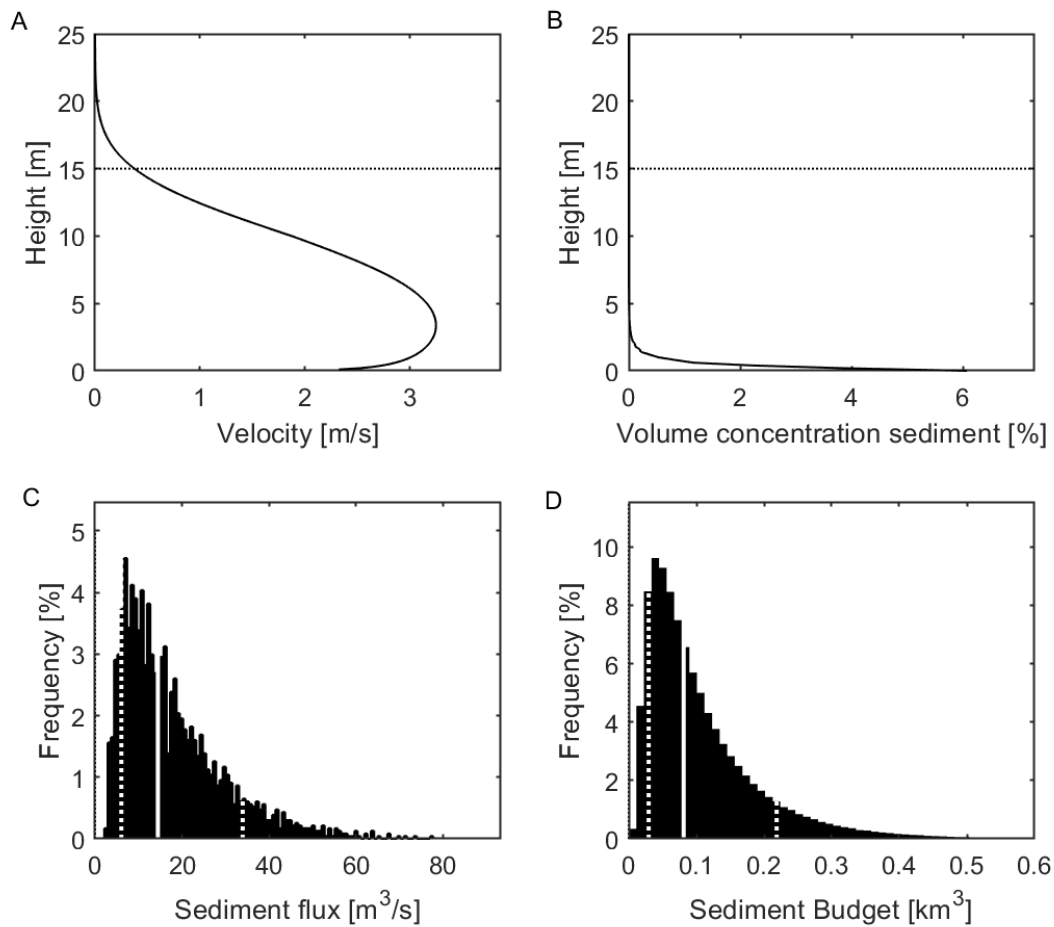
1449 section is determined after intersecting the channel margins with channel depth  $D$ . The bank angle is

1450 set to  $10^\circ$  throughout this paper.



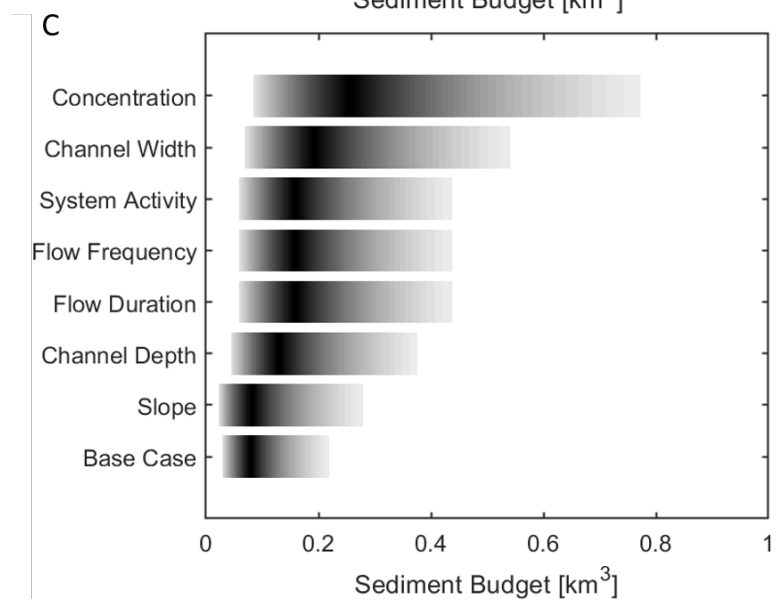
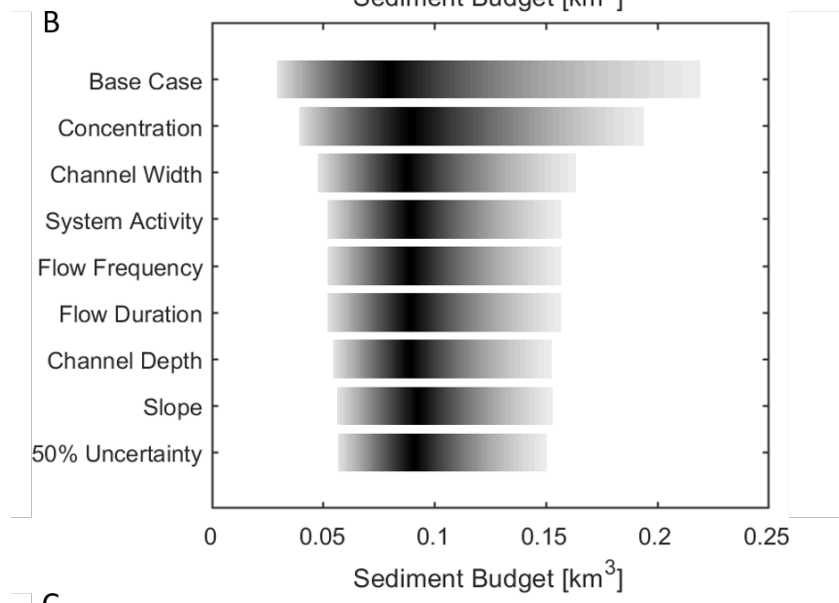
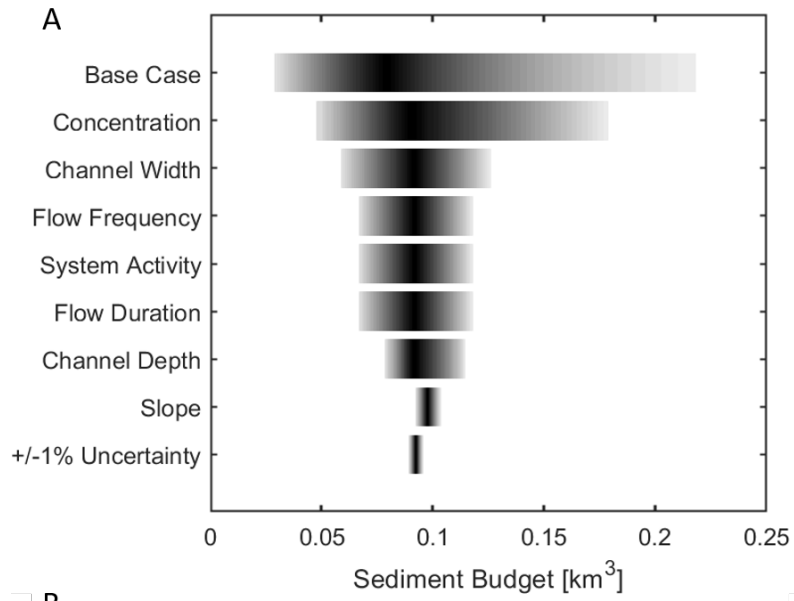
1451

1452 **Fig. 2:** The analytical formulation for the velocity profile of turbidity currents (Eq. 1; solid line), as  
 1453 obtained by subtracting the plane-mixing-layer term (Eq. 5; dash-dotted line) from the logarithmic  
 1454 velocity (Eq. 2; dashed line). Following Kneller et al. (1999) in lieu of Altinakar et al. (1996).

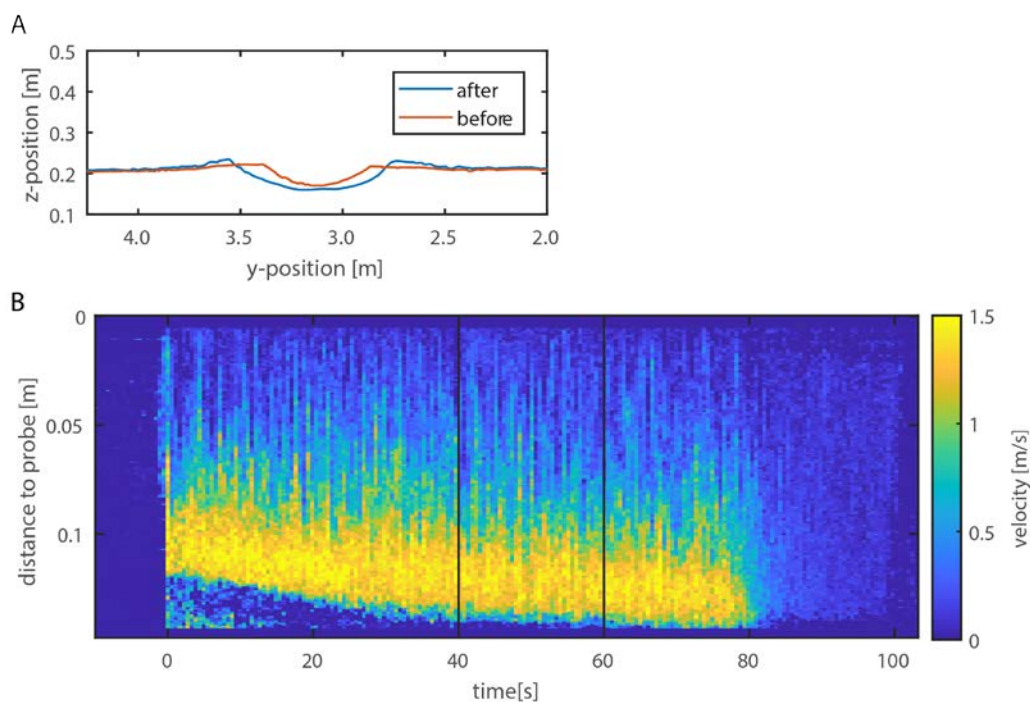


1455

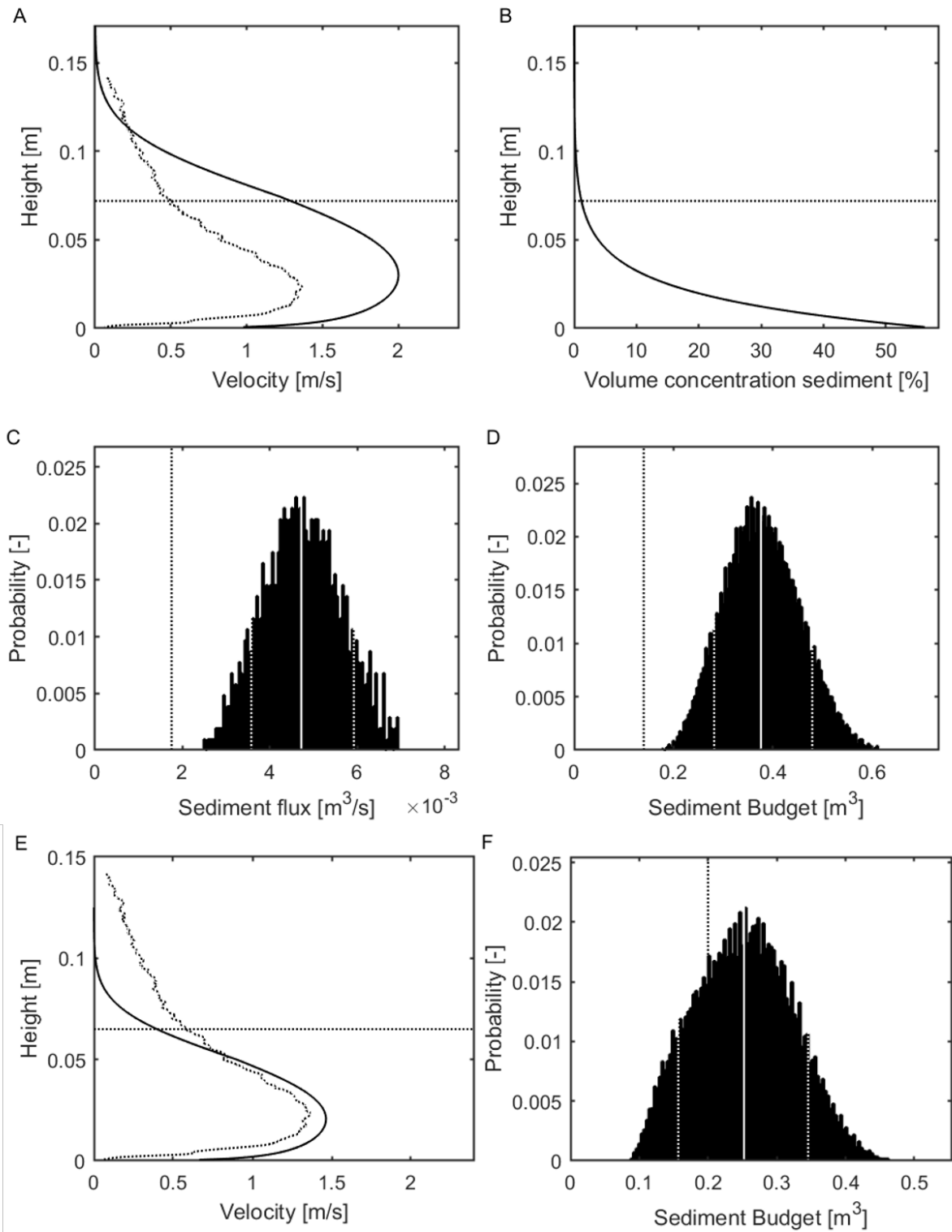
1456 **Fig. 3:** SBE default results for the base case simulation [Table 2]. A&B) Velocity and concentration  
 1457 profiles of a characteristic turbidity current in the base case system. Horizontal dotted line indicates  
 1458 the mean input channel depth for reference. Note that the displayed example was thinner than the  
 1459 mean thickness. C) Histogram of sediment flux (m<sup>3</sup>/s) through a characteristic channel cross section.  
 1460 D) Histogram of sediment budget of the system over a full cycle of activity. Vertical white line  
 1461 indicates the p<sub>50</sub> of predicted sediment budgets, white dotted lines indicate p<sub>10</sub> and p<sub>90</sub>.



1463 **Fig. 4:** Tornado diagrams of sensitivity analyses of the SBE results. Base case conditions are given in  
 1464 Table 2. A) Uncertainty in all variables apart from 1 is reduced to +/-1% of the mean input of the base  
 1465 case. Uncertainty of all variables was reduced in the “+/-1% Uncertainty” scenario. B) Uncertainty of  
 1466 all variables apart from one was reduced to 50% of the uncertainty in the base case. Uncertainty of all  
 1467 variables was reduced in the “50% Uncertainty” scenario. C) Input range of a single variable was  
 1468 doubled compared to the base case. The gray scales changes from black for  $p_{50}$  to light gray for  $p_{10}$   
 1469 and  $p_{90}$ .



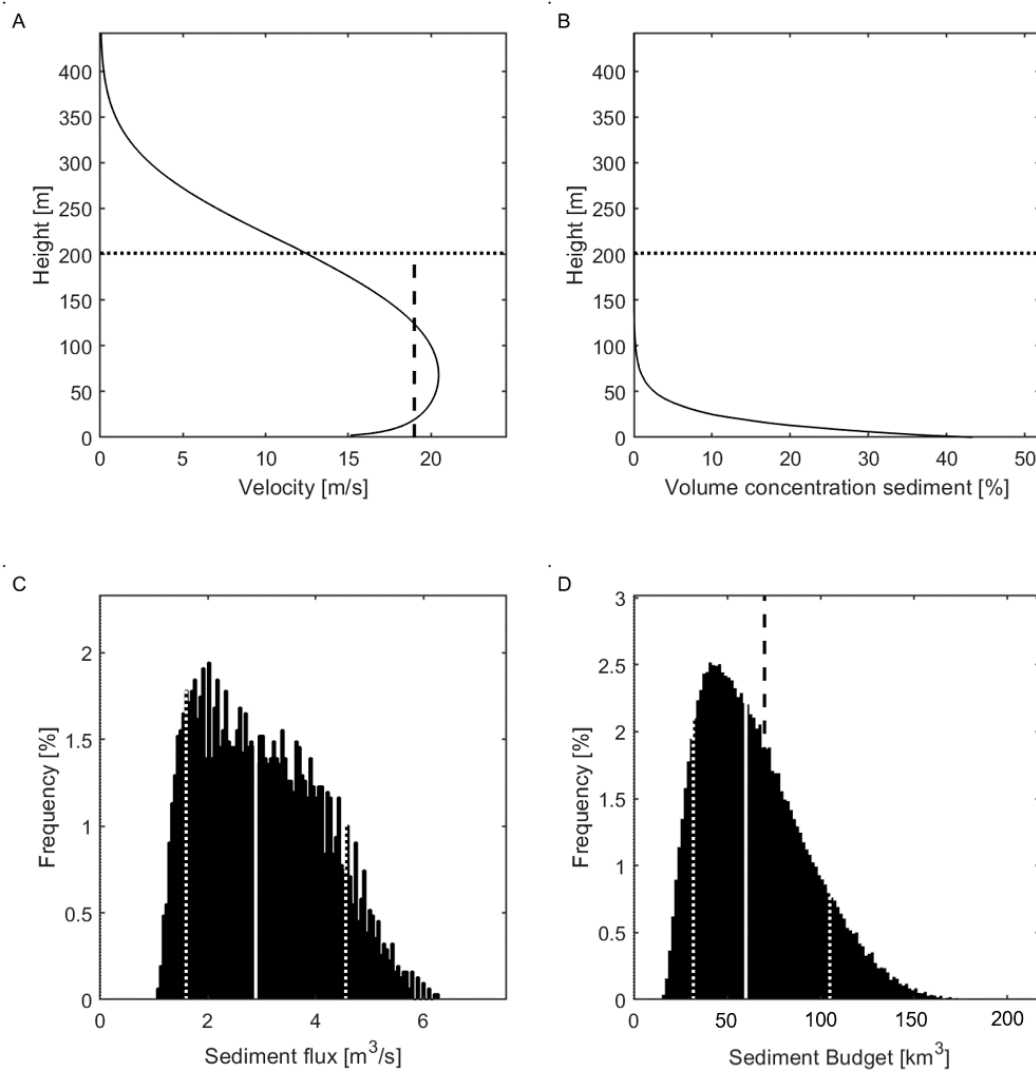
1470  
 1471 **Fig. 5:** A) Channel cross-sections measured before and after Run 3 of de Leeuw et al. (2018b). B)  
 1472 Velocity of the experimental turbidity current measured at the channel thalweg measured with an  
 1473 Ultrasonic Velocimetry Profiler (UVP). The distance from the high-velocity core of the turbidity current  
 1474 to the UVP probe increases during the first 40 seconds of the experiment, which indicates erosion of  
 1475 the channel thalweg. Vertical black lines indicate the 20 s averaging window used for validation of the  
 1476 SBE velocity profile.  
 1477



1478

1479 **Fig. 6:** Results for the SBE simulation of Run 3 of de Leeuw et al. (2018). A) Velocity profile resulting  
 1480 from the SBE (solid line); measured velocity profile (dashed line). Horizontal dotted line indicates  
 1481 channel confinement depth. B) Concentration profile resulting from the SBE. C) Simulated range of  
 1482 sediment flux. Black dotted line indicates sediment flux of the experiment ( $1.9 \cdot 10^{-3} \text{ m}^3/\text{s}$ ). White

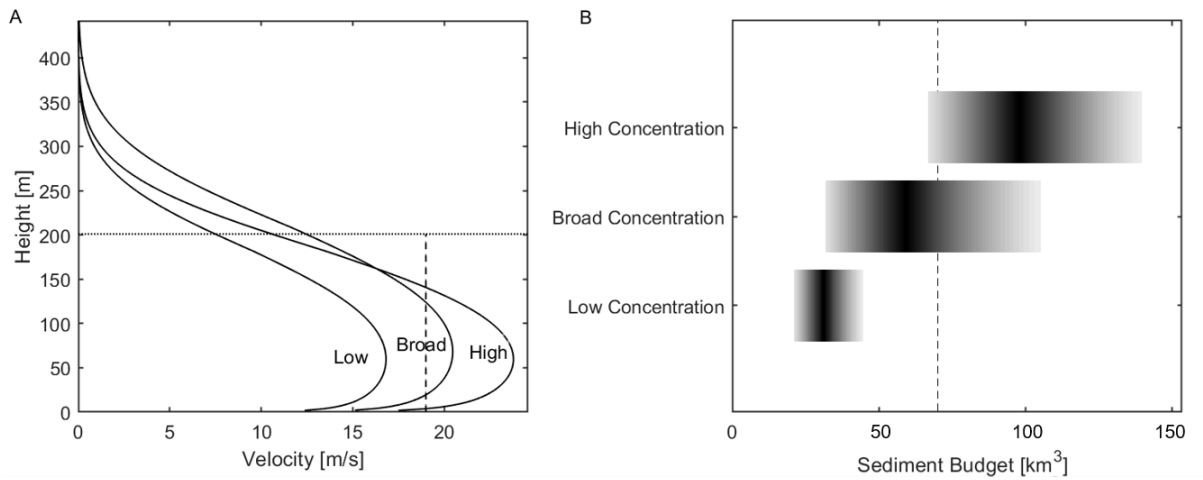
1483 vertical line indicates the median of the reconstructed sediment fluxes ( $3.4 \cdot 10^{-3} \text{ m}^3/\text{s}$ ); dotted lines  
 1484 indicate 10<sup>th</sup> and 90<sup>th</sup> percentiles of reconstructions. D) Reconstructed sediment budget. Black dotted  
 1485 line indicates the amount of sediment supplied to the mixing tank in preparation of Run 3 of de Leeuw  
 1486 et al. (2018b;  $0.15 \text{ m}^3$ ). White vertical line indicates the median of the reconstructed sediment  
 1487 budgets ( $0.27 \text{ m}^3$ ); white dotted lines indicate 10<sup>th</sup> and 90<sup>th</sup> percentiles of simulated budgets.



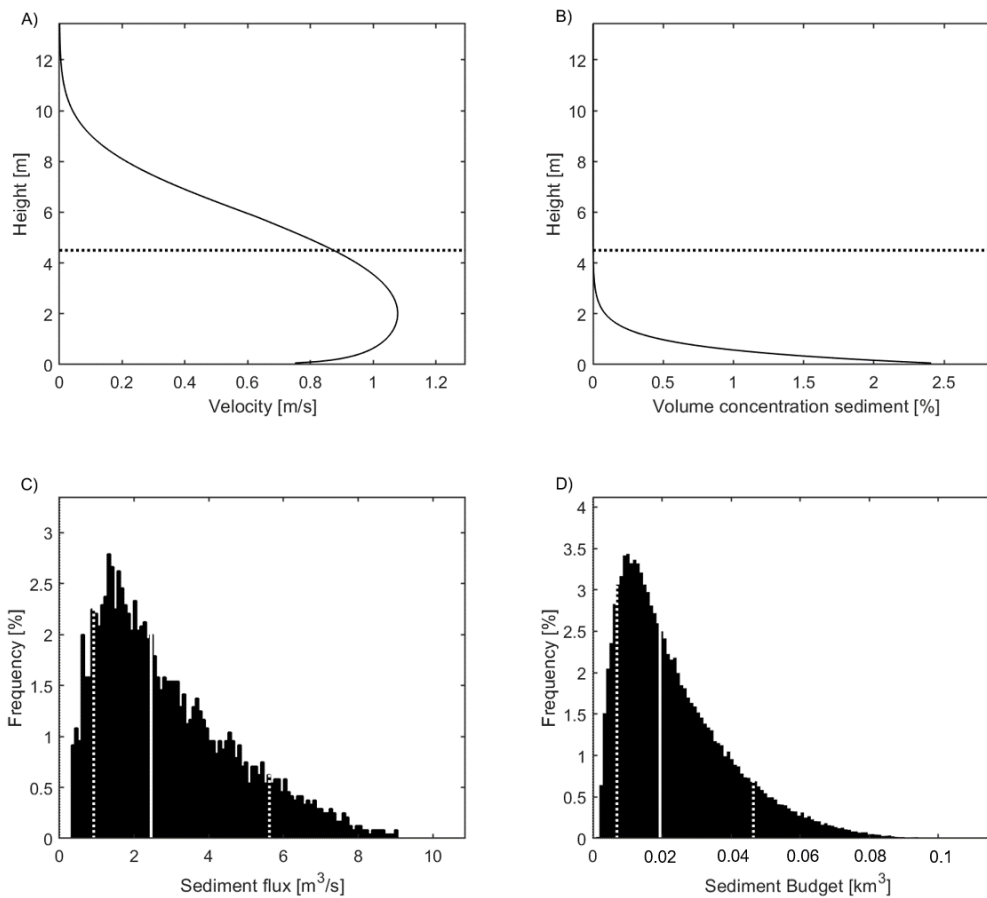
1488  
 1489 **Fig. 7:** SBE results of the Grand Banks 1929 turbidity current reconstruction. A&B) Representative  
 1490 velocity and concentration profiles. Horizontal dotted line indicates flow thickness from Stevenson et  
 1491 al. (2018). Vertical dashed line indicates velocity based on the timing of cable breaks (Heezen &  
 1492 Ewing, 1952). C) Sediment flux. Vertical white line indicates the  $p_{50}$  of predicted sediment flux, white



1493 dotted lines indicate  $p_{10}$  and  $p_{90}$ . D) Simulated sediment budget of the flow through Transect 2.  
 1494 Vertical white line indicates the  $p_{50}$  of predicted sediment budgets, white dotted lines indicate  $p_{10}$  and  
 1495  $p_{90}$ . Vertical black dashed line indicates estimated sediment budget of the Eastern Valley ( $70 \text{ km}^3$ ).

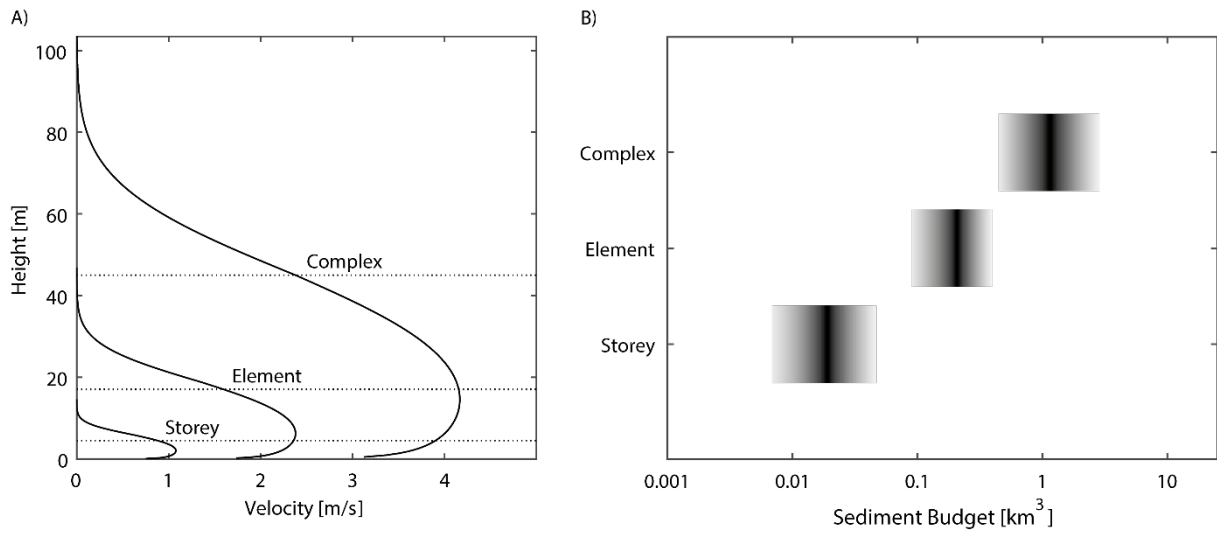


1496  
 1497 **Fig. 8:** A) Examples of characteristic velocity profiles obtained for low concentration estimate (slow  
 1498 flow), broad concentration estimates (intermediate flow), and high concentration estimates (fast  
 1499 flow) of the 1929 Grand Banks turbidity current. Vertical dashed line indicates cable break velocity.  
 1500 B) Simulated sediment budget ranges for the three concentration ranges (see Table 2). Gray scale  
 1501 changes from black at  $p_{50}$  to light gray at  $p_{10}$  and  $p_{90}$ . Vertical dashed line indicates observed 70  
 1502  $\text{km}^3$  sediment budget.



1503

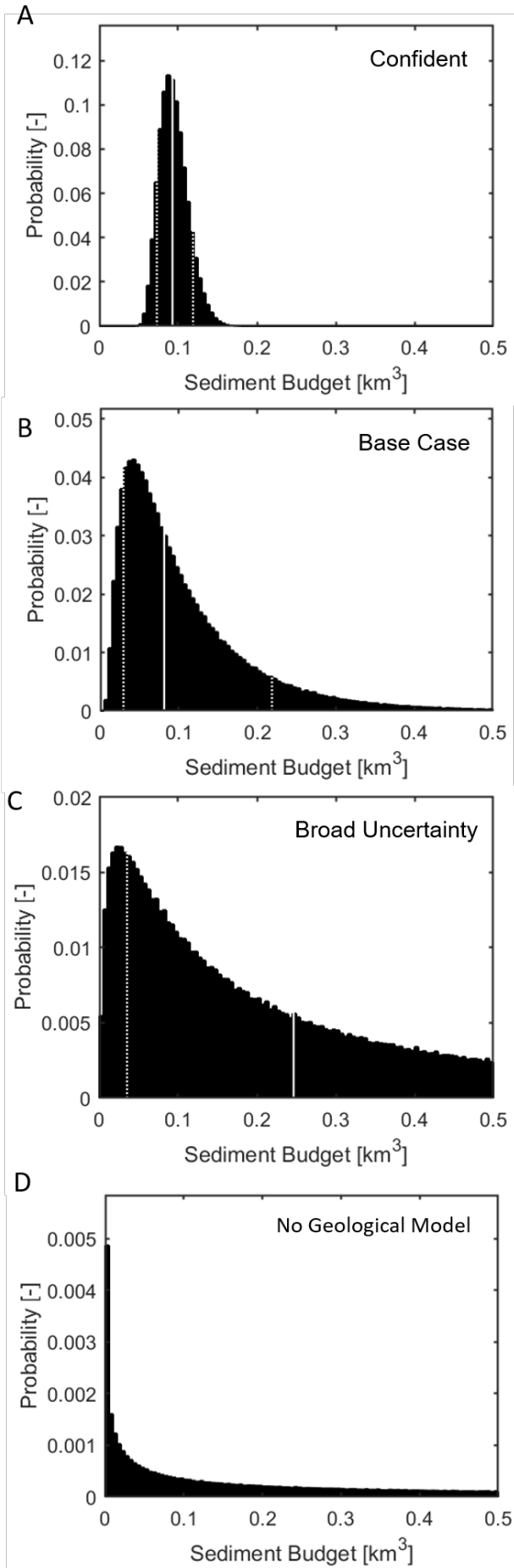
1504 **Fig. 9:** SBE-results for characteristic turbidity currents related to storey-dimensions in Tres Pasos  
 1505 Formation slope channels. A) Velocity profile of one typical simulation, dotted line indicates mean  
 1506 storey-surface depth. B) Sediment concentration profile of one typical simulation. C) Histogram of  
 1507 calculated sediment fluxes through the channel cross-section per second. Vertical white line indicates  
 1508 the  $p_{50}$  of predicted sediment flux, white dotted lines indicate  $p_{10}$  and  $p_{90}$ . D) Histogram of cumulative  
 1509 sediment budget of 500 characteristic turbidity currents. Vertical white line indicates the  $p_{50}$  of  
 1510 predicted sediment budgets, white dotted lines indicate  $p_{10}$  and  $p_{90}$ .



1511

1512 **Fig. 10:** A) Example characteristic turbidity currents resulting from storey dimensions, element

1513 dimensions, and unrealistic complex-dimensions.



1515 **Fig. 11:** *Sediment budget histograms for scenarios with decreasing confidence of interpretation.*  
1516 *Vertical white line indicates the  $p_{50}$  of predicted sediment budgets, white dotted lines indicate  $p_{10}$  and*  
1517  *$p_{90}$ . A) Confident levels of uncertainty with +/-10% ranges around a mean estimates of input*  
1518 *conditions. B) The base case scenario with factor 2-3 differences between minimum and maximum*  
1519 *inputs. C) Broad uncertainty with a factor 5 difference between minimum and maximum inputs. D)*  
1520 *Sediment budget predictions in the absence of a specific geological model.*  
1521

1522 **Table 1.** Overview of possible boundary condition ranges and guiding principles described in the text.

Boundary Condition	Guiding principles			
	Channels		Canyons	
Channel width & depth	Bankfull dimensions		Trimlines / Terraces	
System Slope	Gentle 0.5-1°	Intermediate 1-2.5°	Steep 2.5-6°	Very Steep 6-12°
	Mud-rich 50 µm; 200 µm	Fine Sand 150 µm; 350 µm	Medium-Very coarse sand 500 µm; 1750 µm	Gravel-rich 1250 µm; 5000 µm
	Very Dilute 0.05-0.2%	Dilute 0.2-0.6%	Intermediate 0.6-2%	High 2-5%
Sediment Concentration	Proximal (delta) slope		Distal parts of large (~1000 km) fans	
	Minutes – 1 hour	Slope channels in small basins / Upper continental slope	Large canyons / Lower continental slope	Days- 1 week
Current Duration	Active delta slopes & tidally affected systems	Shelf edge / Narrow shelf systems	Distal active systems	Distal abyssal plain & Seismogenic supply
	Weekly - Monthly	Seasonal	Decadal	Centuries-Millennia
Current Frequency	Active part of the dominant sediment supply cycle [kyr]			
System Activity	Combine with Current Frequency to enforce event count		Combine with Current Frequency to enforce event count	

1523

1524

1525 **Table 2** *Input parameters for the SBE simulations of a hypothetical base case, EuroSEDS experiments,*  
 1526 *and the 1929 Grand Banks turbidity current.*

1527

	Base Case	Eurotank Experiment	Eurotank Experiments Broad ranges	1929 Grand Banks Event
Channel Width [m]	200-400	0.82 +/-10%	0.5-0.8	23000 +/-10%
Channel Depth [m]	10-20	0.072 +/-10%	0.05-0.08	201 +/-10%
System Slope [°]	1-2.5	11 +/-10%	=	0.45 +/-10%
Thalweg grainsize (d <sub>50</sub> ; d <sub>90</sub> ) [*10 <sup>-6</sup> m]	150; 350	131,223	=	1250; 5000
Sediment Concentration [%]	0.2-0.6	15 +/-10%	=	Ref. 2.7-5.4 High 5.4 +/-10% Low 2.7 +/-10%
Current Duration [h]	2-4	80/3600 +/-10%	=	4-8
Current Frequency [-/yr]	0.05-0.1	1	=	1
System Activity [kyr]	5-10	0.001	=	0.001

1528  
 1529  
 1530

1531 **Table 3:** *Input conditions used to simulate characteristic turbidity currents at the storey, element, and*  
 1532 *complex scales in the Tres Pasos Formation*  
 1533

	Scenario Storey	Scenario Element	Scenario Complex
Channel Width [m]	200+/-10%	400+/-10%	800-1000
Channel Depth [m]	2.5-6.5	17+/-10%	30-60
System Slope [°]	0.7-0.9	0.7-0.9	0.7-0.9
Thalweg grainsize (d <sub>50</sub> ; d <sub>90</sub> ) [µm]	200;400	200;400	200;400
Sediment Concentration [%]	0.2-0.6	0.2-0.6	0.2-0.6
Current Duration [h]	3-6	3-6	3-6
Current Frequency [-/yr]	0.1	0.1	0.1
System Activity [kyr]	5	5	5

1534  
 1535



1536 **Table 4:** *The input conditions used to illustrate the effect of scenario confidence on predicted downdip*  
 1537 *sediment volumes.*

1538

	Scenario Confident	Scenario Base Case	Scenario Broad Uncertainty	Scenario No Geological Model
Channel Width [m]	300 +/-10%	200-400	100-500	50-1000
Channel Depth [m]	15 +/-10%	10-20	6-30	2-100
System Slope [°]	1.75 +/-10%	1-2.5	0.5-2.5	0.1-6
Thalweg grainsize (d <sub>50</sub> ; d <sub>90</sub> ) [µm]	150; 350	150; 350	150; 350	150; 350
Sediment Concentration [%]	0.4 +/-10%	0.2-0.6	0.2-1.0	0.05-5
Current Duration [h]	3 +/-10%	2-4	2-10	0.1-240
Current Frequency [- /yr]	0.075 +/-10%	0.05-0.1	0.03-0.15	0.001-1
System Activity [kyr]	7.5 +/-10%	5-10	2-10	0.5-1000

1539

1540

1541